DR. MASSIMILIANO GHINASSI (Orcid ID : 0000-0003-1696-2071)

Article type : Original Manuscript

Reconstruction of an extreme flood hydrograph and morphodynamics of a meander bend in a high-peak discharge variability river (Powder River, USA)

Massimiliano Ghinassi[a] and John Moody[b]

[a] Department of Geosciences, University of Padova, Via G. Gradenigo 6, IT-35131 Padova, Italy (massimiliano.ghinassi@unipd.it

[b] U.S. Geological Survey, 3215 Marine St., Suite E-127, Boulder, Colorado 80303, USA

Associate Editor – Jeff Peakall

Short Title – Extreme flood deposits in a fluvial meander

ABSTRACT

Understanding of morphodynamic processes associated with large-scale floods has recently improved following significant advances of modern technologies. Nevertheless, a clear link between flood discharge and in-channel sedimentation processes remains to be resolved. The hydrological and geomorphological data available for the meandering Powder River (Montana, USA) since 1977 makes it a perfect laboratory to investigate connections between flood discharge and point-bar sedimentation processes. This study focuses on a point-bar that accreted laterally *ca* 70 m during a 50-year recurrence flood, which lasted about 14 days in May 1978. In

September 2018, a trench *ca* 2 m deep and 70 m long was excavated through the axial point-bar deposits, and the 1978 flood deposits were delineated based on georeferenced pre-flood and post-flood cross-section surveys. Sedimentological data show that point-bar deposits accumulated at the early and late flood stages, when the flow was confined to the channel, and have similarities with classical facies models in terms of palaeocurrent patterns and vertical grain-size trend. However, during high-stage flood conditions, when the flow overtopped the bar, cross-cutting of the bar and armouring were typical processes. Integration of sedimentological and palaeo-hydrological data highlight that the relation between channel cross-sectional area and flood discharge play a key role in preserving bar deposits. The integrated approach adopted here provides a basis for advancing palaeoflood hydrology beyond the stage of estimating peak discharges to the next stage of estimating palaeoflood hydrographs.

Keywords: critical shear stress, fluvial sedimentology, lateral accretion, palaeoflood hydrology, point bar, sediment transport

INTRODUCTION

Fluvial meander bends evolve under the effects of concurrent erosional and depositional processes. Erosion along the outer bank allows these bends to shift laterally, and deposition along the inner bank leads to the formation of point-bar deposits, as depicted by numerous field studies since the second half of the past century (Allen, 1963; Bernard & Major Jr, 1963; McGowen & Garner, 1970; Bluck, 1971; Jackson, 1975, 1976a; b; Puigdefabregas & Van Vliet, 1977; Nanson, 1980, 1981). Point bars deposits are formed by lateral stacking of inclined beds (Bridge *et al.*, 1995; Moody & Meade, 2014), which can vary in grain size from mud to gravel (Bridge *et al.*, 1995; Kostic & Aigner, 2007; Simon & Gibling, 2017). Sediment is transported along the bend in a three-dimensional flow configuration, which is characterized by a secondary helical circulation developed downstream of the bend apex (Hooke, 1975; Ferguson *et al.*, 2003; Blanckaert, 2019). This secondary circulation moves sediment from the thalweg zone toward the inner bank, allowing the bar to accrete laterally. Due to the overall decrease of drag forces from the toe to the top of the bar, the coarser particles are commonly concentrated at the toe of the bar, whereas finer particles can reach the bar top (Allen, 1982). This separation of grains or fining-upward grain-size

trend of point bars is described in all the most popular fluvial-facies models (e.g. Allen, 1963; McGowen & Garner, 1970; Bluck, 1971). Different water depth and velocity cause a variable distribution of bedforms and related sedimentary structures. Plane-parallel and cross-stratifications are typical of lower-bar deposits, whereas ripples are more common in upper-bar deposits (Shiers *et al.*, 2019). Point bars accrete at variable rates (Moody, 2019; Ielpi & Lapôtre, 2020) and following different styles of planform transformations, including expansion, translation and rotation (Jackson, 1976b; Durkin *et al.*, 2015; Ghinassi & Ielpi, 2015; Durkin *et al.*, 2019; Russell *et al.*, 2019; Yan *et al.*, 2019), which can give rise to a wide spectrum of stratal architectures that include concave-upward and convex-upward geometries (Smith *et al.*, 2009).

Like other fluvial bars, stratal architecture and distribution of sedimentary facies in point bars are generally constructed when discharge reaches or exceeds bankfull conditions, whereas lower discharges reshape these deposits (Moody & Meade, 2014; Blom *et al.*, 2017; Naito & Parker, 2019; Francalanci *et al.*, 2020; Ielpi *et al.*, 2020). Although the importance of bankfull discharge in constructing bars is largely acknowledged, linking hydrology of river floods with related deposits has been the goal of a limited number of studies (Fielding *et al.*, 1999; Sambrook Smith *et al.*, 2010) and changes in sedimentary processes during floods is still poorly known. This knowledge gap mainly arises from the difficulty in documenting sedimentary processes during floods, when hydraulic properties can be constrained by direct measurements, but deposition cannot be directly observed and measured underwater. Reconstruction of the flood hydrograph from resulting deposits can provide a relevant contribution that links flood dynamics with variability of sedimentary processes.

Palaeoflood hydrology is an outgrowth of flood geomorphology applied to ancient floods (Costa, 1986; Baker, 2008). The primary focus has been on estimating peak-flood discharges to expand data sets for flood-frequency analysis (Costa, 1986; Baker, 2008; Kjeldsen *et al.*, 2014) and climate reconstruction (Knox, 1985). Some physical indicators used to estimate palaeostages are temporary, lasting only weeks to years (for example, organic debris lines and physical effects on vegetation) whereas others are more permanent lasting years to millennia (for example, slack-water deposits, gravel, boulder bar tops and scour lines) (Jarrett, 1990; Benito & O'Connor, 2013), and commonly contribute to identifying and aging series of multiple floods (Benito & O'Connor, 2013). Additionally, recurrence and duration of floods has been demonstrated to exert a relevant

control on fluvial deposition (Fielding *et al.*, 2009, 2018; Plink-Björklund, 2015, 2019; Nicholas *et al.*, 2016; Best & Fielding, 2019), where peak discharge variability can play a crucial role in preservation of fluvial macroforms (Fielding *et al.*, 2018).

Establishing a link between the flood hydrograph and the resulting sedimentary deposits can advance the understanding of ancient fluvial successions and the prediction of river channel processes during extreme floods. In the framework of meandering river systems, understanding point-bar morphodynamics at different discharges will also help to unravel the hydraulics of palaeoflood deposits, and can provide explanations for inconsistencies between classical point-bar facies models and field evidence, such as the observation of coarsening-upward point-bar deposits (Jackson, 1976b; Swan *et al.*, 2019), or the lack of regularly offset, laterally-accreting beds (Moody & Meade, 2014; Johnston & Holbrook, 2019).

The present study focuses on flood deposits that accumulated on a point bar of the meandering Powder River (Montana, USA; Fig. 1A) during an extreme flood, in May 1978. This study reconstructs the flood hydrograph and bar morphodynamics by investigating the sedimentary features of an exceptionally well-preserved, 70 m long, accretionary package formed during the flood and later exposed in an artificial trench. The goal of this study is two-fold: (i) to depict sedimentary features and bar morphodynamics recorded in the 1978 deposits and compare them with classical facies models; and (ii) to reconstruct the flood hydrograph from the particle-size characteristic of the sediment in individual accretionary packets and compare it with the measured hydrographs. This work provides insights into understanding flood deposits in the stratigraphic record and procedures for reconstructing the palaeo-flood hydrograph from sedimentary characteristics.

GEOMORPHOLOGICAL SETTING

Powder River

Powder River flows across the northern high plains of the western United States and drains an area of 34,706 km^2. It begins in the Big Horn Mountains of central Wyoming, flows eastward and then turns northward after exiting the mountains onto the high plains where the bed slope is about 0.001, typical channel width is *ca* 50 m, and the mean daily discharge was 12.5 $m^3\ s^{-1}$ between 1975 and 2017 at the gauging station at Moorhead, Montana (USGS station

06324710, USGS National Water Information System, 2017, Fig. 1A). Powder River is not supply-limited, but transports a wide range of sediment sizes from suspended sand and clay (*ca* two to three million metric tons per year; Moody & Meade, 1990) to bedload consisting of cobbles and sand (*ca* 160,000 metric tons per year; Hembree, 1952). During floods, these suspended and bedload transport rates rise to at least 12,000 kg s^{-1} and 180 kg s^{-1}, respectively, at a water discharge of 300 m^3 s^{-1} (fig. 31 in Hembree, 1952; Moody & Meade, 2008). The high plains have a semi-arid climate, and these hydroclimatic conditions can produce four types of floods each year (Moody & Meade, 2014; Moody, 2019) resulting in a high peak-discharge variability (Fig 2A; coefficient of variance = 1.02, Fielding *et al.*, 2018). Ice-breakup floods are in late winter and spring (February–April) caused by snow and ice melting at low elevations (1000–2000 m) in the southern portion of the basin; snowmelt floods are in the late spring and early summer (May–June) originating at higher elevations (2000–4000 m); localized episodic flashfloods are in the summer (July–September), and occasional autumnal floods are in the fall (September–October). The largest flood on record was an autumnal flood in October 1923 (Fig. 2A; *ca* 2830 m^3 s^{-1}).

The 1978 flood and the study site

The extreme flood of May 1978 was not a typical annual snowmelt flood but combined with an anomalous, stationary atmospheric circulation pattern that fed moisture to the high plains from the Gulf of Mexico (Parrett *et al.*, 1984; Hirschboeck, 1988; Moody & Meade, 2008; Meade & Moody, 2013). This produced extended periods of precipitation during 3 to 8 May and 16 to 19 May amounting to 180 mm of rain or roughly three times the monthly long-term average for May at Broadus, Montana (Fig. 1A) (Parrett *et al.*, 1984; Meade & Moody, 2013). As consequence, the pre-flood discharge (56 m^3 s^{-1}) started to rise at Moorhead and Broadus on 6 May and generated a minor peak in the hydrograph between 9 and 13 May reaching a mean-daily discharge of 103 m^3 s^{-1} on 12 May followed by a waning phase between 13 and 17 May (Fig. 2B). On 17 May water level rose rapidly, exceeded bank-full discharge (*ca* 170 m^3 s^{-1}, Moody & Meade, 2008) near the gauging station at Moorhead (Fig. 1A) on 17 May, peaked at 779 m^3 s^{-1} on 20 May at Moorhead (Fig. 2A and B), and peaked later at 711 m^3 s^{-1} on 21 May at Broadus (Fig. 2B) (Moody & Meade, 2008). On 22 May, measured suspended-sediment concentrations were 41,000 mg L^{-1} at Moorhead and 22,600 mg L^{-1} at Broadus (Parrett *et al.*, 1984; Moody & Meade, 2008, fig. 3). During the flood,

surface water crossed over most of the point bars and flooded a large part of the alluvial plain (Fig. 2D and E), but the deeper water followed the thalweg (Fig. 1B). After 22 May water level fell, and discharge stabilized around 150 m^3 s^{-1} from 24 to 31 May, and then slowly waned until the pre-flood discharge was reached on 28 June 1978.

The study bend and the associated point-bar deposits are located about 24 km south-west of Broadus, Montana (Fig. 1A), where Powder River forms a 0.8 to 1.0 km wide channel belt cut into coal-bearing Palaeocene deposits of the Fort Union Formation (Flores, 1981). The study site is located at a channel cross-section referred to as PR163 (Fig. 1B). Cross-section PR163 was established in 1977 with station 0 about 10 m from the edge of the left bank and marked by a steel reference pin [see more details published by Moody & Meade (1990)]. Horizontal distances and elevations (above NGVD29) were measured in metres from station 0 to a second reference pin at station 75.0 on the right bank (Fig. 2C). This cross-section has been monitored since 1977 and is sited just downriver from the bend apex. The study bend is gently skewed downstream and has a NNW–SSE trending axis (Fig. 3B). Wavelength of the meander bend is *ca* 550 m and sinuosity is *ca* 1.5. At this site in 1977, the outer bank (i.e. left bank) was *ca* 2.5 m above the 1977 thalweg elevation (962.25 m; all elevations are on the line of section, Fig.2C). This outer bank was part of a low-level Lightning terrace (964.73 m, Fig. 1C) in front of a higher Moorcroft terrace (965.67 m, Fig.1C) (Moody & Meade, 2008; Meade & Moody, 2013). The 1978 flood eroded 65 m from the outer bank removing the low-level Lightning terrace (along with the reference pin at station 0), so that after the flood, the 1978 outer bank corresponded to the higher Moorcroft terrace that was *ca* 4.0 m above the 1978 thalweg (961.71 m). Bank erosion was smaller upriver from the bed apex and greater downriver from the apex (Ghinassi *et al.*, 2019), and the bend apex shifted *ca* 100 m downriver (i.e. moving almost transverse to the bend axis). The high-water elevation during the 1978 flood was later surveyed to be 965.52 m. Thus, the maximum water depth at the study site ranged from *ca* 3.3 m (height above 1977 thalweg at station 15, Fig. 2C) to *ca* 3.7 m (height above the 1978 thalweg at station -30, Fig. 2C). On the right bank, floodwater spread across the point bar and floodplain from station 0 to station 650 (Fig. 2C and D).

METHODS

Sedimentological investigations and terminology

The substantial width of the channel erosion and concomitant lateral deposition from the right bank towards the left bank permitted a space-time substitution to determine the temporal sequence of depositional events. To analyze the 1978 flood deposits, a trench was dug across the point bar in 2018 using a backhoe (Fig. 3A). The trench trended 151 N°(magnetic) and was sited about 1 m downriver from the line of section for PR163 (Fig. 3B), which is the only location on the point bar where pre-flood and post-flood topographic data could be used to delineate the 1978 flood deposits. The trench was 70 m long, but only about 2 m deep, because of the presence of the groundwater table, which prevented digging to the base of the bar. Positions in the trench were referenced to the coordinate system described above in *The 1978 flood and the study site* section (Fig. 2C). In this coordinate system, the riverward and landward termination of the trench were sited at station 0 and station 70, respectively.

Stations within the trench were marked by wooden stakes every 2 m and adjusted so that their tops were at 962.3 m above NGVD29. Thus, the high-resolution topographic data from pre-flood and post-flood surveys (Moody & Meade, 1990) could be superimposed on the upriver side of the trench wall to identify the 1978 flood accretionary package (Fig. 4A and C). An earlier GPR survey was conducted to obtain a 3D map of the sediment deposits; however, the post-1978 muddy deposits which top the bar prevented penetration of the signal, and seismic data were not suitable for any analysis.

A total of 644 high-resolution (16 Megapixel) digital photographs were acquired from different angles and merged by means of the Agisoft™ Photo-Scan software to create a 3D photogrammetric model of the upriver side of the trench. The photogrammetric model was used to produce a high-resolution 'orthophoto' on which the 1978 flood accretionary package and its internal stratal surfaces were marked (Fig. 4A). Lateral variation in sediment grain-size distribution and sedimentary structures were also recorded. Palaeocurrent measurements were obtained from cross-strata and imbricated gravels.

Key stratigraphic surfaces, marking erosional events or relevant changes in sediment texture or accretionary style, were used to subdivide the flood accretionary package into four units (Fig. 4B), which were representative of four flood phases. A total of 107 grain-size samples were collected (Fig. 4B). Primary sediment samples (71) were collected near the base of the trench every 1 m from station 0 to station 70. Four additional vertically-spaced samples were

collected above nine of these primary samples and were spaced every 6 m between stations 30 to 62 and at station 65 (Fig. 4B). Particle-sizes were separated into whole phi intervals by hand sieving the >4 mm size classes (Guelfi, 2019; see supplementary material files), and by using a Rotap® machine for 20 minutes for the <4 mm size classes (Guy, 1977). The largest grain size class was 64 to 128 mm, and the smallest class was <0.063 mm. The amount of sample (mass, M in grams) that was analyzed ranged from 59 to 7825 g depending on the degree of sorting. Sorting ranged from moderately sorted (0.6ϕ) to very poorly sorted (2.8ϕ) based on the sorting parameter referred to as the inclusive graphic standard deviation, $\sigma 1$, which was calculated in ϕ units according to Folk & Ward (1957). Larger volume samples were collected in the field when larger particles were present and when the sample appear less well sorted to achieve a representative sample. The relation between the amount of sample, M and the sorting parameter $\sigma 1$ was $M = 1893\sigma 1 - 1418$ ($R^2 = 0.45$) provides a verification of this procedure.

Hydrodynamic reconstruction

In general, as water depth increases, the water moves larger sediment particles. The authors assume that particles stop when the shear stress falls below the critical shear-stress, τ_{cr} [dynes cm^{-2}], which is defined as the minimum shear-stress needed to just begin to move a sediment particle. Thus, knowing the particle-size distribution of deposits accumulated at a specific time and the related critical shear stress, one can invert the problem and estimate the water depth for that specific depositional time. Critical shear-stresses are frequently extracted from the original Shield's curve (Wiberg & Smith, 1987). However, this curve is based on the ideal condition that the sediment size, D (cm), being transported is the same size as the bed material, k_s (cm). If the bed material size, k_s, is much larger than D (i.e. $D/k_s < 1$), then the sediment particle can be trapped in pockets with an angle of repose near 90^o or greater and the critical shear-stress required to move the particle out of such a pocket is greater than that shown on the original Shield's curve. If on the other hand, $D > k_s$ (or $D/k_s > 1$), then the particle can roll easily on a relatively smooth bed and the critical shear-stress is less than that shown on the original Shield's curve.

In order to consider the effects of bed grain-size variability, Wiberg & Smith's (1987) eq. 8 was used for heterogenous particle sizes to calculate the dimensionless critical (*cr*) shear-stress:

$$(\tau_*)_{cr} = \frac{\tau_{cr}}{(\varrho_s - \varrho)gD} \quad (1)$$

where $\rho_S$is the density of the sediment [assumed to be 2.65 g cm^{-3}], ρ is the density of water [1.00 g cm^{-3}] and *g* is the acceleration of gravity [980 cm s^{-2}]. Wiberg & Smith's (1987) eq. 8 is repeated below as Eq. 2:

$$(\tau_*)_{cr} = \frac{2}{(C_D)_{cr} < f^2\left(z/z_0\right) > [1 + \left(F_L/F_D\right)_{cr} tan\phi_0]} \frac{1}{(tan\phi_0 cos\beta - sin\beta)} \quad (2)$$

C_D is the drag coefficient of particle of diameter *D,* which was approximated by a power law function (R^2 = 0.9985) of the particle Reynolds number, *Re*, given by $\log_{10} C_D = a_4X^4 + a_3X^3 + a_2X^2 + a_1X + a_0$, where $X = \log_{10}Re$ and a_4 =-0.0012, a_3 = 0.0142, a_2 = 0.074, a_1 = -0.8953, and a_0 = 1.4213.The expression $<f^2(z/z_0)>$, (cm^2 s^{-2}) is the average of the square of the velocity profile over the particle cross-section calculated using vertical intervals less than *ca D*/20 . F_L is the lift force, [dynes] and F_D is the drag force, [dynes] on the particle calculated using Wiberg & Smith's (1987) eqs 2 and 3. $\phi_0$is the angle of repose of the particle on the bed, which was approximated by using Miller & Byrne's (1966) expression for nearshore sand:

$$\phi_0 = 61.5^o(D/k_s)^{-0.3}. \quad (3)$$

and β is the slope of the bed. The bed slope for the 1978 flood on Powder River was used, which averaged 0.0011 between the gaging stations at Moorhead and Broadus (channel distance = 89 km and Valley distance = 58 km) during 5 to 26 May 1978. Once Eq. 2 is solved by iteration, the critical water-depth is given by:

$$h_{cr} = (\varrho_s - \varrho)gD\frac{(\tau_*)_{cr}}{\varrho g\beta} \quad (4)$$

This critical water-depth was computed using the D_{95} for each grain-size sample, since maximum particle size does not discriminate between samples (i.e. many samples had the same maximum particle size) and also resulted in unrealistically high water depths when compared to

the measured flood stage (Fig. 2B), whereas D_{50} resulted in unrealistically low water depths. The underlying bed sediment sample was the sample beneath the moving sediment sample and the roughness k_s was set equal to D_{84}.

Each grain-size sample was assumed to represent an instant of time during the flood, at which the hydraulic conditions were considered quasi-stationary. A chronological sequence number was assigned to each individual sample based on the stratigraphic relations between samples (Table 1). Additionally, in order to minimize the effects of possible errors in defining this chronological sequence, sedimentological evidence was used to group adjacent samples (for example, group 1.1 in Unit-1; Table 1), and the average critical water-depth was also calculated for each group of samples. A hydrograph was reconstructed by ordering the value of critical water-depth as a function of chronological sequence number of the group.

To compare the reconstructed hydrograph with measured ones, the onset and termination of flood sedimentation at PR163 were estimated by assuming that they were triggered when the bar (i.e. inner bank) was submerged or emerged, respectively. Times of submergence and emergence of the pre-flood and post-flood inner bank at stations 66 and 20 were computed using a simple analytical model based on Manning's equation, the pre-flood and post-flood cross-sectional geometry (Moody & Meade, 1990; Moody & Meade, 2020), the average channel slope (0.0011) and the discharge at the gauging station at Moorhead. There are no tributaries between Moorhead and PR163, and the model predictions have been verified against 49 field observations from 16 cross-sections along the entire 90 km geomorphic study reach from 1980 to 2019 (see Supplementary files).

Thickness of cross-sets was measured from areas with groups of grain-size samples (for example, group 1.1 in Unit-1), in order to get values that were closely spaced in time and space (Leclair & Bridge, 2001;). Thickness values were used to reconstruct primary height of dunes and make water-depth estimations, which were compared with those calculated from bottom shear stress. Since the number of thickness values at each site was limited, the mean dunes height (H_m) was considered to be 2.9 times the mean cross-set thickness (S_m), as proposed by Leclair & Bridge (2001). Water depth (D) was estimated as $D = 6.7H_m$ with a level of uncertainty of +50% (Bradley & Venditti, 2017).

RESULTS

The 1978 deposits

The 1977 and 1978 survey lines were projected onto the trench wall (Fig. 4A). The 1977 line fell within cross-stratified sand and gravel deposits, which stratigraphically overlayed an erosional surface between stations 63 and 67.5 (Fig. 4A). This surface dipped towards the channel at *ca* 15° and cut sandy deposits (Fig. 4C). The 1978 survey lines almost fits the base of a muddy interval (yellow layer in Fig. 4A) that forms the present-day bar top morphology between stations 67.5 and 21 (Fig. 4A). Between stations 21 and 0 the base of this muddy layer descends below the 1978 survey line defining two major depressions centered at stations 13 and 3 (Fig. 4A).

Between the 1977 and 1978 survey lines, the major stratigraphic surfaces define the accretionary package formed during the 1978 flood and show that most of the bar is exposed in the trench (Fig. 2C). The location of the 1977 survey line within cross-stratified sand and gravel deposits suggests that the 1977 bar was eroded during the flood. Specifically, the inner bank retreated from stations 45 to 65 and the channel thalweg lowered *ca* 1 m in the trenched zone. The overall fit of the 1978 survey line with the base of the bar-top muddy interval indicates that the flood accretionary package was mantled and preserved below this mud, which has accumulated over the past four decades. The only significant reworking of the 1978 accretionary package was around stations 3 and 13, where a subsequent flood scoured two depressions in 1980 (Moody & Meade, 1980). Variation of sedimentary features and stratal patterns allow the subdivision of this package into four main units (Figs 5, 6, 7 and 8). Sedimentary features of these units, including variability of cross-set thickness and grain size are summarized in Fig. 9 and Table 1.

Unit-1

Lateral accretionary packets of Unit-1 extended from station 68 to station 45 (Fig. 9B). These deposits were at least 120 cm thick and showed an overall vertical decrease in grain size from coarse (with scattered gravel) to medium-fine sand. Unit-1 was composed of inclined beds dipping riverward (350° N) at *ca* 15 to 20° (Fig. 5A), which were up to 50 cm thick. Sand was primarily cross-stratified (Fig. 5B), although plane-parallel stratification appeared locally. Cross-strata were commonly marked by coal grains (Fig. 5C) eroded from the Palaeocene substrate and

are at the angle of repose (high-angle dunes in Bradley & Venditti, 2017). Cross-strata point to a palaeocurrent direction toward SSE (i.e. almost away from the channel, Fig. 5D). Grain-size analyses revealed that Unit-1 packets mainly consist of relatively sorted sand with scattered gravels (Fig. 5E), and sediment grain size increases moving riverward from station 65 to 49 (Fig. 5F). Cross-sets range in thickness between 8 cm and 37 cm (Groups 1.1, 1.2 and 1.3 in Fig. 9).

Unit-2

Unit-2 was deposited between station 43 and station 20 (Fig. 6A and 9B). The inclined beds of Unit-1 were replaced by a single large set of cross-stratified sand, which was up to 120 cm thick, with a dip azimuth of 30 to 35°N. Between stations 43 and 40, cross-strata were characterized by an increase in dip angle from 10–15° to 25–30°. These packets mainly consisted of medium sand with scattered gravels (Fig. 6G and H) and showed reactivation surfaces along with 10 to 15 cm deep scours filled with cross-stratified sand (Fig. 6A). Palaeocurrent direction of scour-filling sand was consistent with dip azimuth of large cross-strata. Between stations 40 and 32 cross-strata dip at 25 to 30° and were composed of medium to coarse sand with scattered pebbles and cobbles (Fig. 6G and H). Between stations 32 and 20, cross-strata dipped at *ca* 20° and showed a tangential geometry. These packets were characterized by a channelward increase in grain size (Fig. 6H). Gravels included abundant matrix-free layers. Between stations 31 and 26, in the lower part of the trench wall, two mesoforms were embedded at the base of cross-strata (Fig. 6B and D). These mesoforms had a relief of *ca* 35 cm and a wavelength of *ca* 3.5 m, and showed an asymmetrical profile, with the lee side dipping south (210–220°) at *ca* 20° to define a wavy stratification that merges with toe strata of the major cross-set.

Unit-3

Unit-3 was deposited in an erosional depression cut into Units-1 and 2 between stations 60 and 24. It conforms to the inclined beds of Unit-2 between stations 24 and 16 (Figs 4A, 7A and 7B), and is summarized in Fig. 9B. The erosional surface flooring Unit-3 defined a depression between stations 60 and 35 and became sub-horizontal between stations 35 and 24. The erosional depression showed a symmetrical profile (Figs 4A and 7A), with an axis trending *ca* 70°N, and an erosional relief of *ca* 130 cm. This depression was filled up with predominately horizontal-bedded,

trough cross-stratified coarse sands with gravels (Fig. 7C). In the lower part of the infill (stations 43–45 at 120–140 cm below the bar surface) the D_{50} of the sands ranged from 1.08 to 1.88 mm (Fig. 7H, open circles). Whereas in the upper part of the infill (stations 50–38 at 20–30 cm below the bar surface) the D_{50} of the sands were smaller and ranged from 0.48 to 0.75 mm. Where the erosional surface became sub-horizontal, it was covered with plane-parallel stratified coarse sands (D_{50} = 0.89 and 1.08 mm at stations 32 and 26, 35 and 30 cm below the surface, respectively) with gravels. Palaeocurrents from cross-strata and imbricated sands pointed to a flood flow towards *ca* 67.5°N (Fig. 7D). Between stations 24 and 16, the plane-parallel stratified sands dipped down to become conformable to clinoforms of the underlying Unit-2. Inclined beds riverward (350° N) dip at *ca* 15 to 20° and consisted of coarse sands (D_{50} = 0.86–1.53 mm, between stations 17–20 at 120–190 cm below the bar surface) with gravels. Plane-parallel stratification was dominant and included lenses of matrix-free gravels. In the upper part of the bar (*ca* 70–80 cm from the trench base), between stations 22 and 19, some strata dipped at higher angle than underlying ones to define downlap geometries (Fig. 7E). In the same area (station 20), a 15 cm thick layer of planar-cross stratified sand indicates a local flow towards 135°N (Fig. 7F).

Unit-4

Unit-4 extended from station 20 to the northern or riverward termination of the trench at station 0 (Figs 4B, 8A and 9B). It consisted of clinostratified coarse sands (stations 20 to 13; Fig. 8D) grading riverward into horizontally-bedded medium sand and gravels (stations 13 to 0; Fig. 8D). Transition from Unit-3 was defined by an increase in sand content and decrease in grain size of the gravelly fraction. Clinostratified coarse sands were relatively well-sorted (Fig. 8F) between station 11 and station 6 (σ_g ranged from 2.4–2.7 and D_{50} ranged from 0.75–1.79 mm). Riverward of station 6, D_{50} increased to a maximum of 3.85 mm at station 2 followed by an abrupt decrease to medium sand (0.35 and 0.32 mm) at stations 1 and 0, respectively (Fig. 8G). Beds were cross-stratified to plane-parallel stratified, with the cross-strata up to 15 cm thick that indicated a southward-directed flow (Fig. 8B and E) and dip at the angle of repose indicating high-angle dunes (Bradley & Venditti, 2017). Horizontally-bedded sand was plane-parallel stratified (Fig. 8C) and covered a basal layer of poorly exposed, cross-stratified gravelly sand. These sandy deposits were

cut by several erosional scours, which range in depth from 10 to 25 cm, and were filled up with cross-stratified sand (Fig. 8C).

Reconstructed hydrograph

The stratal pattern of the four Units define the styles of bar growth during the flood. They show that lateral accretion dominated in Unit-1 and Unit-2, whereas in Unit-3 there was an early stage of vertical deposition, followed by lateral accretion in Unit-4 (Fig. 9A). This stratal pattern provided the basis for assigning a chronological sequence number to individual samples used for grain-size analyses (Fig. 9A and Table 1) and to merge them into groups, which are assumed to represent deposits accumulated under similar hydraulic conditions (Fig. 9A and Table 1).

Ordering the reconstructed critical water-depths (see *Hydrodynamic reconstruction* section) as a function of chronological sequence number allowed the reconstruction of a pseudo flood hydrograph, which is not a function of time but rather a function of sequence number (Fig. 10A). Values of h_{cr} based on individual samples ranged from 0.1 to 3.0 m (Fig. 10A), and the range of the adjusted flood stages (with 1.0 m subtracted from the arbitrary stage datum to adjusted them to water depth) at Moorhead and Broadus were 0–3.6 m and 0–2.9 m, respectively, between 4 and 24 May 1978 (Fig. 2B). Boxplots obtained from grouped samples (Fig. 10A) provide an estimate of the uncertainty of the reconstructed hydrograph.

The pseudo hydrograph reconstructed based on the individual sediment samples has two minor peaks separated by a trough from the main peak (black line in Fig. 10A). The sediment groups do not resolve these minor peaks but rather a single, broad peak defined by deposits of Unit-1 (groups 1.1 to 1.3 in Fig. 10A, Table 1), with median water depths of 0.13 m, 0.55 m and 0.48 m, respectively. The trough is more clearly defined by sediments accumulated at the beginning of deposition of Unit-2 (groups 2.1 and 2.2 in Fig. 10A), with median water depths of 0.18 m and 0.38 m, respectively. The rising limb of the main peak is defined by the remaining sediments of Unit-2 (groups 2.3 and 2.4 in Figs 9A and 10A), with the median depth of 1.3 m and 2.4 m, respectively. Water depths calculated for sediment packets of Unit-3 and Unit-4 define the falling limb of the main peak, with a median water depth oscillating between 1.1 m and 1.7 m in Unit-3 and a minimal value of 0.47 m in group 4.2.

Thickness of cross-sets is available only for Unit-1 (groups 1.1, 1.2 and 1.3), Unit-3 (groups 3.1 and 3.2) and Unit-4 (group 4.1). Thickness varies between 7 cm and 48 cm, and values increase within Unit-1 but decrease in Units 3 and 4 (Fig. 9C). Reconstructed mean values of dune heights (Leclair & Bridge, 2001) and related reconstructed water depths (Bradley & Venditti, 2017) are shown in Figs 9C and 11, respectively. Based on the reconstructed dune heights, water depth increased from *ca* 3.5 to 6 m during the deposition of Unit-1 and decreased from *ca* 5 to 3 m during the deposition of Units 3 to 4 (Fig. 11).

DISCUSSION

Reconstructing bar morphodynamics by integrating sedimentary facies, stratal architecture and palaeocurrent data

The four depositional units forming the flood accretionary package represent different phases of deposition (Fig. 12), which followed an initial phase of bar erosion documented by the erosional surface underlying the 1978 accretionary package. Survey profiles and stratigraphic evidence indicate that this erosional phase removed some of the pre-flood point-bar deposits (Fig. 12A), causing a retreat of the right bank of about 20 m to station 66 before the onset of sedimentation. Unit-1 documents the earliest phase of deposition when the bar accreted laterally towards the left bank for 21 m to station 45 (Fig. 12B). Channelward-dipping beds with internal cross-stratification match deposits described by classical fluvial point-bar facies models (McGowen & Garner, 1970; Bluck, 1971; Jackson, 1976b; Nanson, 1980). These deposits, along with palaeocurrents diverging at *ca* 120 to 140° from dip azimuth of beds, indicate that sediment was mainly transported by a secondary helical circulation (Termini & Piraino, 2011), which strengthened as the high-velocity core moved closer to the outer bank of the channel (Dietrich & Whiting, 1989; Frothingham & Rhoads, 2003; Kasvi *et al.*, 2013). This secondary circulation transported the finer particles toward the bar top (Parker & Andrews, 1986), generating the fining-upward grain-size trend described for many point bars (Miall, 1994, 1995) and observed in Unit-1. Increase in grain-size and cross-set thickness from stations 67 to 45 documents an increase of flow strength and water depth, respectively, and indicate the early waxing-phase of the flood. The secondary helical circulation in the bar axial zone indicates that the main current impinged on the

outer bank upstream of the bend apex (cf. Kasvi *et al.*, 2013, 2017), but the water level was too low to move the main current across the bar (Ghinassi *et al.*, 2019).

Unit-2 records ongoing accretion of the inner bank under different flow configuration. The increase of the dip angle of the stratal surfaces between stations 43 and 40 documents the turning of the laterally-accreting bar slope into a north-east migrating avalanching front (Fig. 12C). This process is consistent with a surge of sediment that moved along the upstream bar and re-entered the main channel in the apex zone, finding space available for the initiation of an avalanching front forced by local topography. These deposits can be ascribed to a unit bar (cf. forced unit bar; Herbert *et al.*, 2020) that migrated for *ca* 8 m along the study section. Similar deposits are described in the upstream to central zone of point bars of the Endrick River, in Scotland (Bluck, 1971), and also in the Burdekin River (Australia) as falling to intermediate stage, flat-topped bar (Fielding *et al.*, 1999). This type of unit bar (cf. Reesink & Bridge, 2007, 2009, 2011) includes reactivation surfaces (stations 43 and 40), suggesting that, at the early stage of growth, it had superimposed bedforms with heights exceeding 25% of the bar (Reesink & Bridge, 2009). In the central part of the unit bar (stations 40 to 32), the paucity of reactivation surfaces and the scarce sorting within cross-strata fit with transition of superimposed dunes into plane beds after an increase of flood discharge. This progressive increase of flow velocity, and related sediment transport rate, are also consistent with flattening of the bar avalanching front (Reesink & Bridge, 2009) between stations 32 and 28. Although cross-stratified sets developed by unit bars commonly exist for timescales much longer than single floods (Reesink & Bridge, 2007; Herbert *et al.*, 2020), these cross-strata indicate that unit bars can form during part of a single flood, and developed a complex internal architecture following rapid changes in flow configurations. The two mesoforms embedded close to the base of the unit bar (stations 31 to 26) developed as antidunes, according with their internal upstream-dipping cross-strata and wavy stratification (Fielding, 2006; Ono *et al.*, 2020; Wang & Plink-Björklund, 2020), and were preserved by rapid burial by the unit-bar front. The erosional surface at the boundary between Unit-2 and Unit-3 indicates that the flow widened, and a substantial portion of the flow moved across the point bar, eroding a deep scour in the central part of the bar (Fig. 12D). Similar scours are described by McGowen & Garner (1970) as cut channels that can propagate downstream to cutoff the meander bend (cf. Viero *et al.*, 2019). The widening flow would cause a concomitant decrease in the cross-stream water-surface slope and a

shift of the main flow away from the outer bank, stalling the secondary helical circulation of the apex zone (Loveless *et al.*, 2000; Wormleaton *et al.*, 2004) and contributing to the preservation of upper-flow regime structures of Unit-2.

Deposits of Unit-3 and related palaeocurrents point out that sedimentation re-started with accumulation of gravels, which moved across the bar, filling the erosional scour and armouring deposits of Unit-2 (Fig. 12E and F) to generate a coarsening-upward grain-size trend (Ghinassi *et al.*, 2019; Swan *et al.*, 2019). Once the flood started waning, the flow shifted back towards the main channel, drifting gravels from the bar top toward the bar slope and generating downlap geometries between stations 22 and 19. At this stage, a secondary helical circulation was re-established, as attested to by appearance of planar-cross stratified gravel (station 20) indicating stronger cross-stream currents.

Unit-4 records a phase when the secondary helical circulation was re-established, as attested to by accumulation of channelward-dipping beds with internal cross-stratification (stations 20 to 13) documenting a palaeocurrent at *ca* 120 to 140° from dip azimuth of beds (Fig. 12G). This flow configuration allows deposition of fining-upward bar deposits and resembles that recorded by Unit-1. This latest phase of the flood is documented by accumulation of horizontally-stratified sand, which was locally scoured by increases in flow turbulence, that may have been triggered by the presence of obstacles or localized flow confinement.

Critical water depth sensitivity

The critical water-depth was sensitive to the ratio of the size of the moving sediment, D, and the roughness of the bed material, k_s. When $k_s << D$, the critical water-depth was low (for example, h_{cr} = 0.24 m, Table 1, chronological sequence number 1, k_s = 1.04 mm, D = 25.4 mm) because the shallow water-depth could easily roll sediment particles on the relatively smooth bed material. But when k_s was larger ($k_s < D$) the critical water-depth increased (for example, h_{cr} = 1.22 m, Table 1, chronological sequence number 9, k_s = 11.8 mm, D = 26.7mm). For other conditions, $k_s > D$, the critical water-depth was relatively high (for example, h_{cr} = 0.84 m, chronological sequence number 19, k_s = 8.8 mm and D = 4.6 mm) because the particles were almost 'trapped' in the pocket formed by the bed material. The condition $k_s \sim D$ (which is often assumed) produces the

lowest critical water-depth (for example, h_{cr} = 0.12 m, chronological sequence number 20, k_s = 1.5 mm and D = 1.9 mm).

Converting the pseudo flood-hydrograph to an actual flood-hydrograph

The pseudo flood-hydrography is based solely on sediment characteristics. Striking similarities between the shape of the pseudo flood-hydrograph (Fig. 10A) and the measured hydrographs at Moorhead and Broadus during the 1978 flood (Fig. 2B), provide guidance for converting the pseudo flood-hydrograph to an actual flood-hydrograph based on absolute chronological time. Such a conversion can be carried out through identification of specific time-based control points (CP1 to CP6 in Fig. 10B). While reconstructing a pseudo flood-hydrograph from sediment characteristics of the geological record is possible, the conversion to an actual hydrograph is not normally possible. However, we make this step as a means of verifying our reconstruction.

Control point 1 (CP1) was the time of submergence of the inner bank at station 66.0 (elevation 963.3 m, *ca* 40 $m^3 s^{-1}$). This corresponded to 6 May 1978 at *ca* 00:00 hours (Table 1) based on calculations using Manning's equation and the pre-flood 1977 channel profile (see *Hydrodynamic reconstruction* section for method used to estimate submergence and emergence times). The calculations also indicated that for several days after submergence there was sufficient depth over the inner bank (between stations 46.3 to 66.0, Fig. 2C) to cause erosion. Assuming that changes in the cross-sectional profile were small during 6 May, then the corresponding maximum shear stresses would have been *ca* 13 dynes cm^{-2} over the outer edge of the inner bank at station 46.3 (Fig. 2C) and *ca* 58 dynes cm^{-2} over the trough centred at station 58.0 (Fig. 2C). These shear stresses would have been sufficient, initially, to erode 2 mm up to almost 8 mm size particles (τ_{cr} = 13 to 57 dynes cm^{-2}, respectively; Table 7.1, Julien, 1998), and later as the flow deepened, larger particles over a period of about four days.

Control point 2 (CP2) was defined as the onset of deposition of the accretionary flood package starting at station 66, and corresponded to 10 May 1978 at 12:00 hours (Table 1), when the Moorhead and Broadus hydrographs indicated a temporary decrease and stabilization of the flood discharge.

The time of the low-river discharge recorded at Moorhead and Broadus stations on 16 May at 12:00 hours defined control point 3 (CP3), which corresponded to the initiation of the sandy forced unit bar forming Unit-2. Deposition of the *ca* 8 m accreting unit bar of Unit-2 over three to four days would be consistent with the rapid increase of river discharge after CP3 and culminating with the development of antidunes just before the onset of flood-peak erosion.

Control point 4 (CP4) was placed at the end of deposition of Unit-2, just before the shifting of the flow across the bar and downcutting of the erosional surface flooring deposits of Unit-3. Since the shift of the flow across the bar probably happened before the peak discharge on 21 May 1978, CP4 was set to be 20 May 1978 at 12:00 hours (Table 1).

Control point 5 (CP5) was defined by the restart of deposition just after the peak discharge, and was assumed to be on 21 May at 12:00 hours and to correspond to accumulation of the initial deposits of Unit-3 (i.e. group 3.1).

Control point 6 (CP6) was assumed to correspond to the time when deposition ended at the outer edge (i.e. group 3.3) of the inner bank (at station 20, elevation 963.9 m) as it emerged from the water on 23 May at 12:00 hours (based on calculations using Manning's equation and the post-flood 1978 channel profile; see *Hydrodynamic reconstruction* section for method used to estimate submergence and emergence times). The difference in discharge between the submergence of the pre-flood inner bank at station 66.0 (*ca* 40 m^3 s^{-1}) and the emergence of the newly deposited inner bank at station 20.0 (*ca* 170 m^3 s^{-1}) is because the cross-sectional area (measured at bank full relative to the right bank) had increased from *ca* 110 m^2 at the time of submergence to *ca* 250 m^2 at the time of emergence as a result of widening from erosion of the left bank and could thus transport more water.

The control points determine the time intervals between group samples, and thus the absolute time for the reconstructed hydrograph (Fig. 10B). CP1 was fixed by the date of submergence (6 May 1978 *ca* 00:00 hours, Table 1) and represents the beginning of the initial erosion. Between CP2 (10 May 1978) and CP3 (16 May 1978) there are four depositional intervals corresponding to group samples 1.1, 1.2, 1.3 and 2.1. Each time interval was assumed to be one day and 12 hours long. Similarly, the three intervals between CP3 and CP4 (20 May 1978) corresponded to three group samples (2.2, 2.3 and 2.4) were one day and eight hours long. The one-day time interval between CP4 and CP5 (20 to 21 May 1978) corresponds to development of

the erosional surface flooring Unit-3 deposits. Since the cross-sectional area at bank full (right bank) had increased from *ca* 110 m^2 to *ca* 250 m^2, the water elevation and water depth were less for the same discharge after the peak than before the peak discharge (for example, for 100 m^3 s^{-1}, the elevation was estimated to be 963.9 m before and 963.4 m after peak discharge). This change in cross-sectional area promoted deposition. Intervals, during the rapidly falling limb between CP5 and CP6 (23 May 1978), were 16 hours long and corresponded to group samples 3.1, 3.2 and 3.3. Groups 4.1 and 4.2 formed after inner bank emergence, during the latest stage of the waning flood.

The fit of the reconstructed hydrograph with those measured at two stations validates the inverse procedure of using critical shear stress to estimate water depth and provides a comparison for evaluating the procedure of reconstructing water depth from cross-sets (Fig. 11). Although short-term erosion and overlap in thickness distributions of stacked sets commonly hinder detection of peak-flow deposits (Leclair, 2011), the extraordinary accretion rate in this study provided an expanded sedimentary record of the flood, thus allowing the identification of the deposits of group 3.1 as those accumulated close to the flood peak. Cross-strata from these deposits point to a water depth of *ca* 8 m (Figs 9C and 11), whereas the post-flood survey (section 2.2) and the reconstructed hydrograph (Fig. 10B) indicate a maximum water depth of *ca* 3.5 m. A similar overestimation of water depth typifies all other calculations based on cross-set thickness (Fig. 11). Although the relation used to reconstruct dunes formative depth (Bradley & Venditti, 2017) and primary dune height (Leclair & Bridge, 2001) are based on large experimental and natural datasets, the related scaling coefficient does not necessarily represent deposits, which accumulate under high deposition rates during non-steady flow depth and discharge. This inconsistency mainly emerges for reconstruction of the dune height from cross-set thickness, since the scaling relationship by Leclair & Bridge (2001) is mainly consistent with experimental bedforms obtained at constant water depth, and natural bedforms from mid to low peak discharge variability rivers (*sensu* Fielding *et al.*, 2018) like the Calamus and Mississippi River. Accordingly, Bridge (2003) suggests using the Leclair & Bridge (2001) relation for cross-sets accumulated under a negligible depositional rate. Although additional work would be required to test this hypothesis, it appears that a high deposition rate would contribute to preserving most of the study cross-strata, thus decreasing the scale coefficient proposed by Leclair & Bridge (2001).

Estimation of sediment transport rates during the flood

Deposition of the sediment forming part of the flood accretionary package was a function of the lateral or cross-stream (Units 1, 2 and 4) component of the bedload sediment transport rate. An order of magnitude estimate of the downstream bedload rate per unit width in the channel is made by dividing the bedload rate (180 kg s^{-1}; see *Powder River* section) by the typical width of the channel (*ca* 50 m) obtaining a value of 3.6 kg m^{-1} s^{-1}. This is not distributed uniformly across the channel but about eight times more sediment is transported along the outside of the channel near the apex, than on the inside of the channel (Hooke, 1975).

The volume of the sediment in the groups in Units 1 and 2 was *ca* 47 m^3 (*ca* 1 m thick from station 20 to 67). Assuming that the lateral sediment transport was across a unit width of 1 m (in the downstream direction), and using a density of 2650 kg m^{-3}, a sediment concentration of 0.65 gives an estimated mass of *ca* 81,000 kg. The estimated time interval was 10 days for Units 1 and 2 (CP2 to CP4, Table 1), so that an order of magnitude estimate of the lateral or cross-stream sediment transport rate of the secondary flow during the rising stage of the flood would be *ca* 0.09 kg m^{-1} s^{-1}, or *ca* 3% of the streamwise bedload transport rate. These lateral transport rates are associated with daily water discharge of about 90 m^3 s^{-1} (Fig. 9C). Similar lateral rates were measured by Kisling-Møller (1992) in the River Gels Å of western Denmark; a maximum value of *ca* 0.01 kg $m^{-1}s^{-1}$ was estimated from fig. 7 of that study but for a discharge less than bankfull (*ca* 20 m^3 s^{-1}).

During the peak discharge, early on 21 May 1978, the authors assumed that erosion was the dominant process. After this peak, groups in Unit-3 were estimated to be deposited by dune migration in the downstream direction over two days (21 May at 1200 to 23 May at 12:00 hours; Table 1) or during a time interval of *ca* 16 hours per group. Volumes for groups 3.1 and 3.2 were about 13 m^3 (*ca* 1.3 m thick from stations 40 to 50) and 31 m^3 (*ca* 1.3 m thick from stations 38 to 62), with corresponding masses of 22,000 and 54,000 kg. The corresponding sediment-transport rates associated with migration of dunes (at decreasing discharges ranging from *ca* 300 to 150 m^3 s^{-1}) would be 0.4 and 0.9 kg m^{-1} s^{-1} or 11% and 26% of the streamwise bedload transport rate. As a comparison, a paper by Claude *et al.* (2012) gives lateral sediment transport rates by dune tracking on the Loire River in France ranging from 0.03 to 0.15 kg m^{-1} s^{-1}. Bedload transport rate

for deposits of group 3.3 was not calculated, because these deposits accumulated under the interaction between cross-wise and stream-wise processes.

On the falling limb of the hydrograph, the time for the deposition for Unit 4 is not constrained by a control point. If we assume that the two groups in Unit-4 with estimated volumes of *ca* 8 m^3 (*ca* 1 m thick from stations 11 to 19) and *ca* 18 m^3 (*ca* 1.4 m thick from stations 0 to 13) were probably deposited during a two to four day time interval after station 20 (near the riverward end of Unit-3) emerged on 23 May 1978, then the order of magnitude estimate of the lateral sediment transport rates associated with the secondary-flow onto the point bar during the falling stage of the flood would range from 0.08 to 0.36 kg m^{-1} s^{-1} or *ca* 2 to 10% of streamwise transport rate. These latter estimates are associated with daily water discharge of *ca* 150 m^3 s^{-1} (Fig. 9C).

Preservation of flood deposits and implications for fluvial point bar facies models

The reconstruction of the depositional dynamics highlights the key role of the relation between channel cross-sectional area and flood discharge in preserving bar deposits. The limited pre-flood cross-sectional area caused erosion of point-bar deposits during the earliest phase of the flood, even when discharge was an order of magnitude lower than the main peak discharge. The large lateral erosion of the outer bank and the lowering of the channel thalweg created conditions that preserved bar deposits even at highest discharge stages. Additionally, the enlarged channel cross-section shaped by the 1978 flood prevented the bar from experiencing significant erosion by subsequent floods during the past four decades allowing full preservation of the extreme flood deposits. Enlargement of channel cross-sectional area during a large flood provides a relevant mechanism to preserve extreme-flood deposits in high-peak discharge variability rivers (Fielding *et al.*, 2018), where floodwater discharged during low-intensity floods is confined to the deeper part of channels shaped by large events, thus confining the effects of reworking processes. Accordingly, only a few floods (1982, 1984, 1987, 1993 and 1995) inundated the bar top since 1978. Additionally, these floods mantled the 1978 sediment package with cohesive muddy deposits, which contributed to the preservation of the 1978 sediments.

Distribution of sedimentary structures and palaeocurrent indicators within the four units show that flow configuration changed substantially during the 1978 flood, and that sediment transport rates inferred from sedimentary structure at high-flood stage were remarkably different from those at low-flood stage. Some sedimentary characteristics of the accretionary package fit with those of fluvial point bars described by classical facies models, whereas others do not. Accretionary packets of Unit-1 and Unit-4 show strong similarities with the classical models of point-bar formation, being characterized by channelward-dipping beds accreting transverse to the streamwise flow direction (cf. Miall, 1994, 1995). Accretionary packets of Unit-1 and Unit-4 were deposited during the early and final stage of the flood, respectively, when the streamwise flow followed the main channel around the bar generating a secondary helical circulation. Accordingly, these units show an overall fining-upward trend, although they lack classical heterolithic deposits in the upper part of the bar (Durkin *et al.*, 2015), but show textural similarities with sand-dominated point bars (Hartley *et al.*, 2015; Wu *et al.*, 2015; Shiers *et al.*, 2019; Swan *et al.*, 2019). Sedimentary features of Unit-2 and Unit-3, on the contrary, do not fit the classical facies models. Although unit bars are building blocks of compound point bars (Ghinassi *et al.*, 2014), thickness of their cross-set is commonly much less than the height of the associated compound bar (Wu *et al.*, 2016; Swan *et al.*, 2019). Cross-sets of the unit bar forming Unit-2 were almost half of the height of the entire point bar, and accreted towards the channel, whereas most of unit bars are commonly described to migrate either along the channel or towards the bar top (Ielpi & Ghinassi, 2014; Wu *et al.*, 2016). Gravelly deposits of Unit-3 are not described in the upper part of point bars, where erosional-based bodies are commonly associated with chute channels (Ghinassi, 2011; Van Dijk *et al.*, 2012), which are generally much thinner than the whole bar and filled up with fine-grained deposits. Bar-top gravelly deposits, along with palaeocurrents transverse to the bar axis, indicate that floodwater overtopped the main bar body (Gay *et al.*, 1998) triggering armoring processes and the development of coarsening-upward grain-size trends. The process of bar overtopping has been largely disregarded by many studies, but it can lead to accumulation of deposits with stratal architecture and sedimentary structures that strongly differ from classical point-bar models, especially in fluvial systems characterized by exceptional floods (i.e. high peak-discharge variability systems; Fielding *et al.*, 2018).

CONCLUSIONS

Investigation of point-bar deposits accumulated along the inside of a meander bend of Powder River (Montana, USA) during an extreme flood in 1978 provided data to reconstruct the flood hydrograph and to identify the morphodynamic evolution of the bar during the flood. Using sediment data from the axial part of the bar, specific depositional processes have been ascribed to different flood stages. The similarity between the reconstructed hydrograph and those measured at two stations during the flood validates the proposed sedimentological model.

The major insights derived from this study can be summarized as follows:

1 The relation between channel cross-sectional area and flood discharge plays a key role in preserving bar deposits. The channel cross-sectional area enlarged by the extreme flood, facilitated the preservation of the bar deposits during subsequent floods.

2 During the early and final phases of deposition of the extreme flood, when the flow was confined to the channel, the accumulated deposits were similar to those of classical facies-models in terms of palaeocurrent patterns and vertical grain-size trend.

3 During the phase of peak discharge water overtopped and eroded the bar with a significant reorganization of flow patterns, which produced: (i) the development of upper-flow regime bedforms; (ii) localized cross-cutting of the bar; (iii) armouring of the bar (development of a coarsening-upward grain-size trend); and (iv) widespread formation of gravelly dunes.

4 The definition of a chronological sequence of flood depositional units was critical for the flood hydrograph re-construction. This allowed specific temporal control points to be established based on changes in the depositional units and resulting in a close correlation between the reconstructed and measured hydrographs.

5 Estimates of particle-size characteristics of the bed material was essential for computing physically realistic shear stresses and critical water-depths to reconstruct the flood hydrograph. D_{95} was used to characterize the moving sediment particles, and D_{84} was found best to characterize the bed material.

6 Estimates of lateral bedload transport rate caused by secondary helical circulation ranged from 2 to 10% and lateral bedload transport caused by dune migration ranged from 11 to 26% of the streamwise bedload transport rate.

The integrated sedimentological and hydrological approaches adopted in this paper provide a basis for advancing palaeoflood hydrology beyond the stage of estimating peak discharges to the next stage of estimating palaeo-flood hydrographs. Water depth estimation from shear stress appears as an alternative approach to the use of cross-set thickness, especially for fluvial deposits accumulated under a high depositional condition.

ACKNOWLEDGEMENTS

We would like to acknowledge Bob Meade (USGS, Scientist Emeritus) whose desire to understand sediment moving and storage in the 1970s resulted in a long-term geomorphic data set that started fortuitously just before the 1978 flood. Additionally, the field efforts by Deborah Martin (USGS, Scientist Emeritus), who took detailed notes and Matteo Guelfi, who completed the sediment particle size analyses in about one week of *ca* 0.2 metric ton of samples, which were essential to the reconstruction of the flood hydrograph. The delicate surgical skill of the backhoe operator, Floyd Huckins, who carved a straight, vertical trench wall through unstable sand and gravel as well as through small-scale mud laminae features. Associate Editor J. Peakall, C. Fielding and two anonymous reviewers as well as Jim Pizzuto are kindly acknowledged for commenting and improving the manuscript.

REFERENCES

Allen, J.R.L. (1963) The classification of cross-stratified units. With notes on their origin. *Sedimentology*, **2**, 93–114.

Allen, J.R.L. (1982) Sedimentary Structures. Their Character and Physical Basis. Volume II, Elsevier. 1–663 pp.

Baker, V.R. (2008) Paleoflood hydrology: Origin, progress, prospects. *Geomorphology*, **101**, 1–13.

Benito, G. and **O'Connor, J.** (2013) Quantitative Paleoflood Hydrology. In: *Treatise on Geomorphology* (Ed. J. Shroder and E. Wohl), 9, 459–474.

Bernard, H.A. and **Major Jr, C.F.** (1963) Recent Meander Belt Deposits of the Brazos River: An Alluvial. *Am. Assoc. Pet. Geol. Bull.*, **47**, 350.

Best, J.L. and **Fielding, C.R.** (2019) Describing fluvial systems: Linking processes to deposits and stratigraphy. In: *River to Reservoir: Geoscience to Engineering, Geological Society of London, Special Publications* (Ed. P.W.M. Corbett, A. Owen, A.J. Hartley, S. Pla-Pueyo, D. Barreto, C. Hackney, and S.J. Kape), 488, 151–166.

Blanckaert, K. (2019) Hydro-sedimentological processes in meandering rivers. In: *Fluvial Meanders and Their Sedimentary Products in the Rock Record* (Ed. M. Ghinassi, L. Colombera, N.P. Mountney, A.J. Reesink, and M. Bateman), *John Wiley & Sons, Ltd*, Hoboken, 297–319.

Blom, A., **Arkesteijn, L.**, **Chavarrías, V.** and **Viparelli, E.** (2017) The equilibrium alluvial river under variable flow and its channel-forming discharge. *J. Geophys. Res. Earth Surf.*, **122**, 1924–1948.

Bluck, B.J. (1971) Sedimentation in the meandering river Endrick. *Scottish J. Geol.*, **7**, 93–138.

Bradley, R. W. and **Venditti, J. G.** (2017) Reevaluating dune scaling relations. *Earth-Science Reviews*, **165**, 356–376.

Bridge, J.S., **Alexander, J.**, **Collier, R.E.L.L.**, **Gawthorpe, R.L.** and **Jarvis, J.** (1995) Ground-

penetrating radar and coring used to study the large-scale structure of point-bar deposits in three dimensions. *Sedimentology*, **42**, 839–852.

Bridge. J.S. (2003) Rivers and Floodplains: Forms, Processes, and Sedimentary Record. *John Wiley & Sons*, Malden, Massachusetts (491 pp.).

Claude, N., **Rodrigues, S.**, **Bustillo, V.**, **Bréhéret, J.G.**, **Macaire, J.J.** and **Jugé, P.** (2012) Estimating bedload transport in a large sand-gravel bed river from direct sampling, dune tracking and empirical formulas. *Geomorphology*, **179**, 40–57.

Costa, J.E. (1986) A history of paleoflood hydrology in the United States, 1800-1970. *Eos, Trans. Am. Geophys. Union*, **67**, 425–430.

Dietrich, W.E. and **Whiting, P.** (1989) Boundary Shear Stress and Sediment Transport In River Meanders of Sand and Gravel. In: *River Meandering, American Geophysical Union Water Resources Monograph* (Ed. G. Ikeda, S., Parker), 12, 1–50.

Durkin, P.R., **Hubbard, S.M.**, **Boyd, R.L.** and **Leckie, D.A.** (2015) Stratigraphic Expression of Intra-Point-Bar Erosion and Rotation. *J. Sediment. Res.*, **85**, 1238–1257.

Durkin, P.R., **Hubbard, S.M.**, **Smith, D.G.** and **Leckie, D.A.** (2019) Predicting heterogeneity in meandering fluvial and tidal-fluvial deposits: The point bar to counter point bar transition. In: *Fluvial Meanders and Their Sedimentary Products in the Rock Record* (Ed. M. Ghinassi, L. Colombera, N.P. Mountney, A.J. Reesink, and M. Bateman), *John Wiley & Sons, Ltd*, Hoboken, 231–249.

Ferguson, R.I., **Parsons, D.R.**, **Lane, S.N.** and **Hardy, R.J.** (2003) Flow in meander bends with recirculation at the inner bank. *Water Resour. Res.*, **39**.

Fielding, C. R., Alexander, J., McDonald, R., Smith, N. D., and **Rogers, J.** (1999). Sedimentary facies from ground-penetrating radar surveys of the modern, upper Burdekin River of north Queensland, Australia: consequences of extreme discharge fluctuations. In: F*luvial sedimentology VI*. International Association of Sedimentologists Special Publications. Vol. (Ed. N. D. Smith, and J. Rogers) 28, 347-362

Fielding, C.R. (2006) Upper flow regime sheets, lenses and scour fills: Extending the range of architectural elements for fluvial sediment bodies. *Sediment. Geol.*, **190**, 227–240.

Fielding, C.R., **Alexander, J.** and **Allen, J.P.** (2018) The role of discharge variability in the formation and preservation of alluvial sediment bodies. *Sediment. Geol.*, **365**, 1–20.

Fielding, C.R., **Allen, J.P.**, **Alexander, J.** and **Gibling, M.G.** (2009) Facies model for fluvial systems in the seasonal tropics and subtropics. *Geology*, **37**, 623–626.

Flores, R.M. (1981) Coal deposition in fluvial paleoenvironments of the Paleocene Tongue River Member of the Fort Union Formation, Powder River Area, Powder River Basin, Wyoming and Montana. *SEPM Spec. Publ.*, **31**, 169–190.

Francalanci, S., **Lanzoni, S.**, **Solari, L.** and **Papanicolaou, A.N.** (2020) Equilibrium Cross Section of River Channels With Cohesive Erodible Banks. *J. Geophys. Res. Earth Surf.*, **125**, 1–28.

Frothingham, K.M. and **Rhoads, B.L.** (2003) Three-dimensional flow structure and channel change in an asymmetrical compound meander loop, Embarras River, Illinois. *Earth Surf. Process. Landforms*, **28**, 625–644.

Folk, R.L. and **Ward, W.C.** (1957) Brazos River Bar: A study in the significance of grain size parameters. *Journal of Sedimentary Petrology*, **27**, 3-26.

Gay, G.R., **Gay, H.H.**, **Gay, W.H.**, **Martinson, H.A.**, **Meade, R.H.** and **Moody, J.A.** (1998) Evolution of cutoffs across meander necks in Powder River, Montana, USA. *Earth Surf. Process. Landforms*, **23**, 651–662.

Ghinassi, M. (2011) Chute channels in the Holocene high-sinuosity river deposits of the Firenze plain, Tuscany, Italy. *Sedimentology*, **58**, 618–642.

Ghinassi, M. and **Ielpi, A.** (2015) Stratal Architecture and Morphodynamics of Downstream-Migrating Fluvial Point Bars (Jurassic Scalby Formation, U.K.). *J. Sediment. Res.*, **85**, 1123–1137.

Ghinassi, M., **Ielpi, A.**, **Aldinucci, M.** and **Fustic, M.** (2016) Downstream-migrating fluvial point

bars in the rock record. *Sediment. Geol.*, **334**, 66–96.

Ghinassi, M., **Moody, J.A.** and **Martin, D.** (2019) Influence of extreme and annual floods on point-bar sedimentation: Inferences from Powder River, Montana, USA. *Bull. Geol. Soc. Am.*, **131**, 71–83.

Ghinassi, M., **Nemec, W.**, **Aldinucci, M.**, **Nehyba, S.**, **Ozaksoy, V.**, **Fidolini, F.**, **Özaksoy, V.** and **Fidolini, F.** (2014) Plan-form evolution of ancient meandering rivers reconstructed from longitudinal outcrop sections. *Sedimentology*, **61**, 952–977.

Guelfi, M. (2019) Il record sedimentario di un evento estremo di piena in ambiente di barra di meandro fluviale: un esempio dal Powder River (Montana, USA). University of Padova

Guy, H.P. (1977) Techniques of Water-Resources Investigations of the United States Geological Survey, Chapter C1. Laboratory theory and methods for sediment analysis. 58 pp.

Hartley, A.J., **Owen, A.**, **Swan, A.**, **Weissmann, G.S.**, **Holzweber, B.I.**, **Howell, J.**, **Nichols, G.** and **Scuderi, L.** (2015) Recognition and importance of amalgamated sandy meander belts in the continental rock record. *Geology*, **43**, 679–682.

Hembree, C.H. (1952) Sedimentation and chemical quality of water in the Powder River drainage basin, Wyoming and Montana. *US Department of the Interior, Geological Survey*, 92 pp.

Herbert, C.M., **Alexander, J.**, **Amos, K.J.** and **Fielding, C.R.** (2020) Unit bar architecture in a highly-variable fluvial discharge regime: Examples from the Burdekin River, Australia. *Sedimentology*, **67**, 576–605.

Hirschboeck, K.K. (1988) Flood hydroclimatology. In: *Flood geomorphology* (Ed. V.R. Baker, R.C. Koche, and P.C. Patton), *John Wiley & Sons*, New York, 27–49.

Hooke, R.L.B. (1975) Distribution of sediment transport and shear stress in a meander bend. *J. Geol.*, **83**, 543–565.

Ielpi, A. and **Ghinassi, M.** (2014) Planform architecture, stratigraphic signature and morphodynamics of an exhumed Jurassic meander plain (Scalby Formation, Yorkshire, UK).

Sedimentology, **61**, 1923–1960.

Ielpi, A. and **Lapôtre, M.G.A.** (2020) A tenfold slowdown in river meander migration driven by plant life. *Nat. Geosci.*, **13**, 82–86.

Ielpi, A., Lapôtre, M. G., Finotello, A., Ghinassi, M., and **D'Alpaos, A.** (2020). Channel mobility drives a diverse stratigraphic architecture in the dryland Mojave River (California, USA). *Earth Surface Processes and Landforms*, **45**, 1717-1731.

Jackson, R.G. (1975) Velocity-bed-form-texture patterns of meander bends in the lower Wabash River of Illinois and Indiana. *GSA Bull.*, **86**, 1511–1522.

Jackson, R.G. (1976a) Largescale ripples of the lower Wabash River. *Sedimentology*, **23**, 593–623.

Jackson, R.G.I. (1976b) Depositional Model of Point Bars in the Lower Wabash River. *J. Sediment. Petrol.*, **46**, 579–594.

Jarrett, R.D. (1990) Hydrologic and Hydraulic Research in Mountain Rwers. *Water Resour. Bull.*, **26**, 419–429.

Johnston, S. and **Holbrook, J.** (2019) Toggling between expansion and translation: the generation of a muddy-normal point bar with an earthquake imprint. In: *Fluvial Meanders and Their Sedimentary Products in the Rock Record. International Association of Sedimentologists, Special Publication* (Ed. M. Ghinassi, L. Colombera, N.P. Mountney, and A.J.H. Reesink), 48, 47–80.

Julien, P.Y., 1998. Erosion and Sedimentation. Cambridge University Press (280 pp).

Kasvi, E., **Laamanen, L.**, **Lotsari, E.** and **Alho, P.** (2017) Flow patterns and morphological changes in a sandy meander bend during a flood-spatially and temporally intensive ADCP measurement approach. *Water*, **9**, 106.

Kasvi, E., **Vaaja, M.**, **Alho, P.**, **Hyyppä, H.**, **Hyyppä, J.**, **Kaartinen, H.** and **Kukko, A.** (2013) Morphological changes on meander point bars associated with flow structure at different discharges. *Earth Surf. Process. Landforms*, **38**, 577–590.

Kisling-Møller, J. (1992) Lateral sediment transport by bedforms in a meander bend. *Earth Surf. Process. Landforms*, **17**, 501–513.

Kjeldsen, T.R., **Macdonald, N.**, **Lang, M.**, **Mediero, L.**, **Albuquerque, T.**, **Bogdanowicz, E.**, **Bra´zdil, R.**, **Castellarin, A.**, **David, V.**, **Fleig, A.**, **Gu¨l, G.O.**, **Kriauciuniene, J.**, **Kohnova´, S.**, **Merz, B.**, **Nicholson, O.**, **Roald, L.A.**, **Salinas, J.L.**, **Sarauskiene, D.**, **S˘raj, M.**, **Strupczewski, W.**, **Szolgay, J.**, **Toumazis, A.**, **Vanneuville, W.**, **Veijalainen, N.** and **Wilson, D.** (2014) Documentary evidence of past floods in Europe and their utility in flood frequency estimation. *J. Hydrol.*, **517**, 963–973.

Knox, J.C. (1985) Responses of floods to Holocene climatic change in the upper Mississippi Valley. *Quat. Res.*, **23**, 287–300.

Kostic, B. and **Aigner, T.** (2007) Sedimentary architecture and 3D ground-penetrating radar analysis of gravelly meandering river deposits (Neckar Valley, SW Germany). *Sedimentology*, **54**, 789–808.

Leclair, S.F., and **Bridge, J.S**. (2001) Quantitative interpretation of sedimentary structures formed by river dunes. *J. Sediment. Res*. **71**, 713–716.

Leclair, S.F. (2011) Interpreting fluvial hydromorphology from the rock record: large-river peak flows leave no clear signature. In *From river to rock record: the preservation of fluvial sediments and their subsequent interpretation. SEPM Spec. Publ.* **97**, 113–123.

Loveless, J.H., **Sellin, R.H.J.**, **Bryant, T.B.**, **Wormleaton, P.R.**, **Catmur, S.** and **Hey, R.** (2000) The effect of overbank flow in a meandering river on its conveyance and the transport of graded sediments. *Water Environ. J.*, **14**, 447–455.

McGowen, J.H. and **Garner, L.E.** (1970) Physiographic Features and Stratification Types of Coarse-Grained Pointbars: Modern and Ancient Examples. *Sedimentology*, **14**, 77–111.

Meade, R.H. and **Moody, J.A.** (2013) Erosional and Depositional Changes Wrought by the Flood of May 1978 in the Channels of Powder River , Southeastern Montana. 1–29 pp.

Miall, A.D. (1994) Reconstructing fluvial macroform architecture from two-dimensional outcrops:

examples from the Castlegate Sandstone, Book Cliffs, Utah. *J. Sediment. Res. B Stratigr. Glob. Stud.*, **B64**, 146–158.

Miall, A.D. (1995) Description and interpretation of fluvial deposits: a critical perspective. *Sedimentology*, **42**, 379–379.

Miller, R. L., and **R. J. Byrne, R.J.** (1966) The angle of repose for a single grain on a fixed rough bed, *Sedimentology* 6, 303-314,

Moody, J.A. (2019) Dynamic relations for the deposition of sediment on floodplains and point bars of a freely-meandering river. *Geomorphology*, **327**, 585–597.

Moody, J.A. and **Meade, R.H.** (2008) Terrace aggradation during the 1978 flood on Powder River, Montana, USA. *Geomorphology*, **99**, 387–403.

Moody, J.A. and **Meade, R.H.** (1990) Channel changes at cross sections of the Powder River between Moorhead and Broadus, Montana, 1975-88. 252 pp.

Moody, J.A. and **Meade, R.H.** (2014) Ontogeny of point bars on a river in a cold semi-arid climate. *Bull. Geol. Soc. Am.*, **126**, 1301–1316.

Naito, K. and **Parker, G.** (2019) Can Bankfull Discharge and Bankfull Channel Characteristics of an Alluvial Meandering River be Cospecified From a Flow Duration Curve? *J. Geophys. Res. Earth Surf.*, **124**, 2381–2401.

Nanson, G.C. (1980) Point bar and floodplain formation of the meandering Beatton River, northeastern British Columbia, Canada. *Sedimentology*, **27**, 3–29.

Nanson, G.C. (1981) New evidence of scroll-bar formation on the Beatton River. *Sedimentology*, **28**, 889–891.

Nicholas, A.P., **Sambrook Smith, G.H.**, **Amsler, M.L.**, **Ashworth, P.J.**, **Best, J.L.**, **Hardy, R.J.**, **Lane, S.N.**, **Orfeo, O.**, **Parsons, D.R.**, **Reesink, A.J.H.**, **Sandbach, S.D.**, **Simpson, C.J.** and **Szupiany, R.N.** (2016) The role of discharge variability in determining alluvial stratigraphy. *Geology*, **44**, 3–6.

Ono, K., **Plink-Björklund, P.**, **Eggenhuisen, J.T.** and **Cartigny, M.J.B.** (2020) Froude supercritical flow processes and sedimentary structures: New insights from experiments with a wide range of grain sizes. *Sedimentology*, 1–30.

Parker, G. and **Andrews, E.D.** (1986) On the time developmentof meander bends. *J. Fluid Mech.*, **162**, 139–156.

Parrett, C., **Carlson, D.D.**, **Craig, G.S.** and **Chin, E.H.** (1984) Floods of May 1978 in southeastern Montana and northeastern Wyoming. In: *U.S. Geological Survey Professional Paper*, *US Government Printing Office*, 1244, 74.

Plink-Björklund, P. (2019) Latitudinal controls on river systems: implications of precipitation variability. In: *Latitudinal Controls on Stratigraphic Models and Sedimentary Concepts* (Ed. C.M. Fraticelli, P.J. Markwick, A.W. Martinius, and J.R. Suter), *Society for Sedimentary Geology*, 108, 59–81.

Plink-Björklund, P. (2015) Morphodynamics of rivers strongly affected by monsoon precipitation: Review of depositional style and forcing factors. *Sediment. Geol.*, **323**, 110–147.

Puigdefabregas, C. and **Van Vliet, A.** (1977) Meandering stream deposits from the Tertiary of the Southern Pyrenees. *Fluv. Sedimentol. Mem. 5*, **5**, 469–485.

Reesink, A.J.H. and **Bridge, J.S.** (2007) Influence of superimposed bedforms and flow unsteadiness on formation of cross strata in dunes and unit bars. *Sediment. Geol.*, **202**, 281–296.

Reesink, A.J.H. and **Bridge, J.S.** (2009) Influence of bedform superimposition and flow unsteadiness on the formation of cross strata in dunes and unit bars - Part 2, further experiments. *Sediment. Geol.*, **222**, 274–300.

Reesink, A.J.H. and **Bridge, J.S.** (2011) Evidence of bedform superimposition and flow unsteadiness in unit-bar deposits, South Saskatchewan river, Canada. *J. Sediment. Res.*, **81**, 814–840.

Russell, C.E., **Mountney, N.P.**, **Hodgson, D.M.** and **Colombera, L.** (2019) A novel approach for

prediction of lithological heterogeneity in fluvial point-bar deposits from analysis of meander morphology and scroll-bar pattern. In: *Fluvial Meanders and Their Sedimentary Products in the Rock Record* (Ed. M. Ghinassi, L. Colombera, N.P. Mountney, A.J. Reesink, and M. Bateman), *John Wiley & Sons, Ltd*, Hoboken, 385–417.

Sa**mbrook Smith, G. H., Best, J. L., Ashworth, P. J., Lane, S. N., Parker, N. O., Lunt, I. A., Thomas, R. E.** and **Simpson, C. J.** (2010). Can we distinguish flood frequency and magnitude in the sedimentological record of rivers?. *Geology*, **38**, 579-582.

Shiers, M.N., **Mountney, N.P.**, **Hodgson, D.M.** and **Colombera, L.** (2019) Controls on the depositional architecture of fluvial point-bar elements in a coastal-plain succession. In: *Fluvial Meanders and Their Sedimentary Products in the Rock Record* (Ed. M. Ghinassi, L. Colombera, N.P. Mountney, A.J. Reesink, and M. Bateman), *John Wiley & Sons, Ltd*, Hoboken, 15–46.

Simon, S.S.T. and **Gibling, M.R.** (2017) Fine-grained meandering systems of the lower permian clear fork formation of north-central Texas, USA: Lateral and oblique accretion on an arid plain. *Sedimentology*, **64**, 714–746.

Smith, D.G., Hubbard, S., Leckie, D., and **Fustic, M.**, 2009. Counter point bars in modern meandering rivers: recognition of morphology, lithofacies and reservoir significance, examples from Peace River, AB, Canada. *Sedimentology,* **56**, 1655-1669.

Swan, A., **Hartley, A.J.**, **Owen, A.** and **Howell, J.** (2019) Reconstruction of a sandy point-bar deposit: implications for fluvial facies analysis. In: *Fluvial Meanders and Their Sedimentary Products in the Rock Record* (Ed. M. Ghinassi, L. Colombera, N.P. Mountney, A.J. Reesink, and M. Bateman), *John Wiley & Sons, Ltd*, Hoboken, 445–474.

Termini, D. and **Piraino, M.** (2011) Experimental analysis of cross-sectional flow motion in a large amplitude meandering bend. *Earth Surf. Process. Landforms*, **36**, 244–256.

Van Dijk, W.M., **Van De Lageweg, W.I.** and **Kleinhans, M.G.** (2012) Experimental meandering river with chute cutoffs. *J. Geophys. Res. Earth Surf.*, **117**, 1–18.

Viero, D.P., **Dubon, S.L.** and **Lanzoni, S.** (2019) Chute cutoffs in meandering rivers: formative mechanisms and hydrodynamic forcing. In: *Fluvial Meanders and Their Sedimentary Products in the Rock Record* (Ed. M. Ghinassi, L. Colombera, N.P. Mountney, A.J. Reesink, and M. Bateman), *John Wiley & Sons, Ltd*, Hoboken, 201–229.

Wang, J. and **Plink-Björklund, P.** (2020) Variable-discharge-river macroforms in the Sunnyside Delta Interval of the Eocene Green River Formation, Uinta Basin, USA. *Sedimentology*, **67**, 1914–1950.

Wiberg, P.L. and **Smith, J.D.** (1987) Calculations of the critical shear stress for motion of uniform and heterogeneous sediments. *Water Resour. Res.*, **23**, 1471–1480.

Wormleaton, P.R., **Sellin, R.H.J.**, **Bryant, T.**, **Loveless, J.H.**, **Hey, R.D.** and **Catmur, S.E.** (2004) Flow structures in a two-stage channel with a mobile bed. *J. Hydraul. Res.*, **42**, 145–162.

Wu, C., **Bhattacharya, J.P.** and **Ullah, M.S.** (2015) Paleohydrology and 3D Facies Architecture of Ancient Point Bars, Ferron Sandstone, Notom Delta, South-Central Utah, U.S.A. *J. Sediment. Res.*, **85**, 399–418.

Wu, C., **Ullah, M.S.**, **Lu, J.** and **Bhattacharya, J.P.** (2016) Formation of point bars through rising and falling flood stages: Evidence from bar morphology, sediment transport and bed shear stress. *Sedimentology*, **63**, 1458–1473.

Yan, N., **Colombera, L.**, **Mountney, N.P.** and **Dorrell, R.M.** (2019) Fluvial point-bar architecture and facies heterogeneity and their influence on intra-bar static connectivity in humid coastal-plain and dryland fan systems. In: *Fluvial Meanders and Their Sedimentary Products in the Rock Record* (Ed. M. Ghinassi, L. Colombera, N.P. Mountney, A.J. Reesink, and M. Bateman), *John Wiley & Sons, Ltd*, Hoboken, 475–508.

FIGURE CAPTIONS

Fig. 1. Powder River in north-eastern Wyoming and south-eastern Montana. (A) Location of study site between the stream gauging stations at Moorhead, Montana (U.S. Geological Survey [USGS] Station number 06324500) and Broadus, Montana (USGS Station number 06324710). (B) Topographic map (contour elevations are in feet) of a reach of Powder River showing the 1977 channel along with the extent of the inundation by the flood of 1978 (light blue). Red arrows indicate the general downvalley direction of the surface flood waters. Black arrows indicate the flow direction at low discharge or the direction of the deeper water confined to the main channel under the surface water during a flood. Yellow dots are labelled with the distance in kilometres (KM) following the river downstream from the Moorhead Bridge at PRKM 0 in 2016. Adapted from plate 1 of Meade & Moody (2013). (C) Comparison between the pre-flood (1976) and post-extreme flood (1978) planform configuration of meander bend at PR163 with the line of section shown as a black line. In the 1978 photograph, the dotted white line is the bank edge in 1976

Fig. 2. Powder River discharge and the 1978 extreme flood. (A) Daily discharge of Powder River at Moorhead, Montana (USGS Station number 06324500), from 1929 through to 2019. The dashed line at 170 m^3sec^{-1} is an estimate of bankfull flow near the Moorhead gaging station. (B) Hydrograph of the 1978 flood at Moorhead and Broadus. (C) Profile of the surface topography at PR163 trench. Black dotted line is the bar topography in 1977. Black dashed line is the 1978 topography after the flood, and black line is the 2018 topography (just before excavation of the trench in 2018). The blue horizontal line shows the maximum water height during the 1978 flood. (D) Oblique aerial south-westerly view of Powder River looking upstream on 25 May 1978, during the falling limb of the 1978 flood. Red arrow points to the approximate location of the outer bank of the river bend at cross-section PR163. Photograph by R.H. Meade. (E) Oblique aerial view (25 May 1978) looking north-westerly towards the left bank of a bend of the river (about 30 km downriver from the bend at cross-section PR163). Red arrows indicate the general direction of downvalley flood flows across the point bar. Black arrows indicate the flow directions in the low-water channel. Photograph by R.H. Meade.

Fig. 3. The study site. (A) The 151 N° (magnetic) trending study trench. Photograph is taken from the channel, and the upstream trench wall is on the right-hand side. Person for scale is 1.92 m tall standing at about station 0. Backhoe is at about station 73. (B) Present-day (2018) configuration of the meander bend at PR163. Stationing (in metres) is measured from a zero reference pin driven about 1 m into the ground on the left bank in 1977 (pin was lost during 1978 flood). Additional reference pins were installed at station 50.0 and station 75.0. Location of the trench is shown between station 0 and station 70.

Fig. 4. The 1978 flood accretionary package and its internal structure are shown as viewed upriver. (A) Stratal architecture of the accretionary package emphasizing the upper and lower boundaries. (B) Internal partition of the accretionary package in four units. (C) Correspondence between stratigraphic surfaces marking relevant lithological changes and topographic points surveyed on bar top before and after the 1978 flood.

Fig. 5. Deposits of Unit-1. (A) Stratal architecture and sedimentary structures. (B) Cross-strata overlying the erosional surface at station 63.5 (elevation 962.95 m). (C) Cross-stratified sand bearing abundant coal fragments at station 55 (elevation 962.92 m). (D) Palaeocurrents from cross-strata. The black segment indicates extent of Unit-1 within the trench wall. (E) Grain-size cumulative distribution plot. Average D_{50} + standard deviation and average D_{95} + standard deviation is shown as grey boxes. (F) D_{50} particle-size distribution, and (G) particle-size sorting.

Fig. 6. Deposits of Unit-2. (A) Stratal architecture and sedimentary structures. (B) Close view of the central part of Unit-2 (stations 37 to 26). Note the progressive increase in grain size moving towards the right-hand side of the photograph (riverward). (C) Close view of the erosional surface separating steeply-dipping strata of Unit-2 from overlying sandy gravels Unit-3 at station 34 (elevation 963.5 m). Spatula is 25 cm high. (D) Wavy mesoforms (oblique view) between stations 31 and 26 in the lower part of the unit. Measuring stick is 50 cm long. (E) Palaeoflow direction (black arrow) for the cross-set forming Unit-2. The black segment indicates extent of Unit-2 within the trench wall. (F) Reactivation surfaces and scour-fill deposits at station 38. Measuring stick is 20 cm long. (G) Grain-size cumulative distribution plot for samples from Unit-2.

Average D_{50} + standard deviation and average D_{95} + standard deviation are shown as grey boxes. (H) Particle-size sorting and (I) D_{50} grain size at different stations within Unit-2.

Fig. 7. Deposits of Unit-3. (A) and (B) Stratal architecture and sedimentary structures. (C) Erosional surface (red line) separating gravelly deposits of Unit-3 from underlying sandy beds of Unit-1 between stations 50 and 44. (D) Palaeocurrents from cross-strata. The black segment indicates the extent of Unit-3 within the trench wall. (E) Clinostratified gravels at the riverward termination of Unit-3 (stations 20 to 23). Note the downlapping strata around station 22 in the upper part of the bar. (F) Cross-strata documenting a palaeoflow towards the south-east. (G) Grain-size cumulative distribution plot. Average D_{50} + standard deviation and average D_{95} + standard deviation are shown as grey boxes. (H) D_{50} particle-size distribution, and (I) particle-size sorting.

Fig. 8. Deposits of Unit-4. (A) Stratal architecture and sedimentary structures. (B) Sandy cross-strata documenting a flow towards the south at station 15 (elevation 961.5 m). Measuring stick is 50 cm long. (C) Plane-parallel stratified sand overlying scour-fill sand at station 9 (elevation 962.0 m). (D) Gravelly-sand deposits of Unit-4 covered by post-flood muddy deposits accumulated since 1978 between stations 16 and 10. (E) Palaeocurrents from cross-strata. The black segment indicates extent of Unit-4 within the trench wall. (F) Grain-size cumulative distribution plot. Average D_{50} + standard deviation and average D_{95} + standard deviation are shown as grey boxes. (G) D_{50} particle-size distribution, and (H) particle-size sorting.

Fig. 9. The 1978 sediment deposits. (A) Summary of the main groups of sediment samples within different units. (B) Sedimentological, architectural and palaeoflow features of the 1978 flood deposits. (C) Thickness of cross-set in different deposits and related reconstruction of dune height and water depth.

Fig. 10. Reconstruction of the 1978 flood hydrograph. (A) Pseudo hydrograph showing the predicted average critical water-depth at PR163 based on sedimentological characteristics as a function of chronological sequence numbers. Depth is based on the critical shear stress for

deposition of D_{95} sediment in transport over an underlying bed characterized by D_{84}. Solid black circles correspond to individual accretionary packets. Blue-shaded boxplots correspond to groups in Fig. 9A. The black curve is a five-point running average fit to the individual accretionary packets (black circles) and was added to aid in visualization of the pseudo hydrograph. (B) Time-based hydrograph compared with measured hydrographs at Moorhead and Broadus, Montana. Six time-based control points (CP1–CP6, see text for definition criteria) are used to determine the absolute time for each group shown as blue-shaded box plots. The discharge hydrograph is shown as a grey line with a scale on the right-hand axis.

Fig. 11. Comparison between reconstructed water depths obtained from cross-strata and shear stress.

Fig. 12. Reconstruction of bar morphodynamics during the 1978 flood. (A) Initial phase of inner bank retreat and erosion of the pre-flood point bar. (B) Onset of point bar deposition and accumulation of channelward-dipping beds of Unit-1. (C) Development and north-eastward migration of unit bar forming Unit-2. (D) and (E) Erosional phase of Unit-1 and Unit-2 and initial deposition of Unit-3 sediments in the scour trough. (F) Filling of the scour trough with gravelly deposits of Unit-3. (G) Deposition of channelward-dipping beds of Unit-4.

Table 1. Particle sizes and critical water–depth values used to reconstruct the flood hydrograph

[sta., station in metres from left bank zero; depth, distance below ground level in centimetres; CP, control point; na, angle of repose >90°; h, water depth; H, dune cross-set height]

Chrono-logical seq-uence number	Deposited sediment, sample ID	Underlying sediment Sample ID	$D = D_{95}$	$k_s = D_{84}$	D/k_s	Critical water depth, h_{cr}	Group ID	Median group critical water depth, h_{cr}	Deposited sediment sample D_{84}	D_{50}	D_{16}		Absolute time
	(sta.depth)	(sta.depth)	(mm)	(mm)	(--)	(cm)		(m)	(mm)	(mm)	(mm)		
								0.0				CP1	5/6/78 0:00
													erosion
					Unit 1							CP2	5/10/78 12:00
1	65.52	66.55	25.4	1.04	24.5	23.6			9.1	0.42	0.21		
2	64.55	65.37	3.74	0.25	15.1	4.2			1.7	0.71	0.24		
3	63.90	64.55	0.77	1.74	0.4	13.7	1.1	0.13	0.5	0.35	0.20		
4	62.90	63.90	3.9	0.48	8.1	6.6			1.7	0.74	0.26		
5	61.90	62.90	1.3	1.73	0.7	12.9			0.9	0.48	0.26		
6	60.95	61.90	3.1	0.88	3.6	9.4			1.4	0.70	0.30		
7	59.95	60.95	21.2	1.35	15.7	26.3			11.8	1.73	0.52		
8	58.85	59.95	15.6	11.8	1.3	115	1.2	0.55	3.7	0.67	0.24		
9	57.85	59.95	26.7	11.8	2.3	122			15.2	0.92	0.33		
10	56.87	56.110	8.2	7.5	1.1	73.0			3.4	0.80	0.31		
11	55.105	56.87	7.2	3.4	2.1	37.2			3.3	0.78	0.33		
12	54.100	55.105	23.3	3.3	7.2	47.9			2.1	0.47	0.23		
13	53.105	55.105	23.0	3.3	7.1	47.6			10.6	0.91	0.38		
14	52.107	53.105	22.6	10.6	2.1	111	1.3	0.48	1.9	0.65	0.34		
15	51.115	52.107	24.0	1.9	12.4	33.8			8.6	0.95	0.43		
16	50.100	52.107	14.8	1.9	7.7	20.1			7.5	1.57	0.48		
17	49.120	50.135	42.2	13.5	3.1	135			13.8	1.58	0.50		
					Unit 2								
18	43.140	49.120	15.9	13.8	1.2	134			8.8	1.23	0.39		
19	42.150	43.140	4.6	8.8	0.5	84.2			1.5	0.70	0.35		
20	41.150	42.150	1.9	1.5	1.2	12.2			0.9	0.44	0.27		
21	40.145	41.150	14.7	0.9	15.9	18.1	2.1	0.18	4.8	0.59	0.28		
22	39.150	40.145	1.7	4.8	0.4	51.6			0.8	0.40	0.26		
23	38.140	39.150	2.4	0.8	3.1	7.46			0.7	0.38	0.22		
24	37.150	38.140	7.2	0.7	9.7	12.3			0.9	0.41	0.25		
												CP3	5/16/78 12:00
25	36.150	37.150	12.1	0.9	13.4	17.1			1.0	0.45	0.27		
26	35.130	36.150	15.3	1.0	15.8	19.2			1.8	0.60	0.31		
27	34.150	35.130	15.1	1.83	8.3	29.1	2.2	0.38	2.9	0.53	0.29		
28	33.140	34.150	39.4	2.90	13.6	47.3			14.8	0.74	0.33		
29	32.130	33.140	24.3	14.8	1.6	145			9.4	0.96	0.38		
30	31.140	32.130	15.7	9.42	1.7	92			6.9	0.97	0.37		
31	30.140	31.140	48.8	6.94	7.0	84.3			27.2	6.32	0.45		
32	29.140	30.140	51.4	27.2	1.9	235			11.5	0.79	0.33		
33	28.150	29.140	16.6	11.5	1.4	119	2.3	1.3	7.0	0.99	0.41		
34	27.140	28.150	46.4	7.0	6.7	84.6			15.3	1.54	0.49		
35	26.135	27.140	44.0	15.3	2.9	150			14.9	0.88	0.35		
36	25.125	26.135	48.6	14.9	3.3	144			20.4	1.12	0.44		
37	24.140	25.125	103.7	20.4	5.1	175			30.8	1.39	0.46		
38	23.140	24.140	44.0	30.8	1.4	266			16.8	1.09	0.49		
39	22.135	23.140	51.9	16.8	3.1	160	2.4	2.4	28.0	2.85	0.63		

40	21.140	22.135	52.8	28.0	1.9	239			29.7	2.44	0.60			
41	20.150	21.140	14.0	29.7	0.5	296			4.9	0.84	0.43			
												CP4	5/20/1978 12:00	
													erosion	
					Unit 3							CP5	5/21/1978 12:00	
42	44.130	49.120	29.4	13.8	2.1	185			15.9	4.26	0.47			
42	44.110	49.120	16.7	13.8	1.2	132			8.10	1.60	0.55			
42	45.130	49.120	22.4	13.8	1.6	139			8.53	1.88	0.48			
42	46.120	49.120	9.6	13.8	0.7	130	3.1	1.3	3.51	1.08	0.48			
42	47.115	49.120	15.8	13.8	1.1	133			5.62	0.84	0.38			
42	48.125	49.120	10.6	13.8	0.8	131			3.18	0.84	0.38			
42	50.70	49.120	23.0	13.8	1.7	138			10.8	1.03	0.45			
43	56.33	56.63	4.6	2.00	2.3	21.1			1.49	0.75	0.40			
43	50.20	50.50	3.8	19.6	0.2	na			1.30	0.73	0.40			
43	50.50	50.70	28.1	10.8	2.6	113			19.6	1.75	0.47			
43	44.30	44.60	1.0	1.2	0.8	8.5			0.85	0.48	0.25			
43	44.60	44.85	4.1	30.6	0.1	na			1.23	0.44	0.19			
43	44.85	44.110	52.8	8.1	6.5	93.9	3.2	1.1	30.6	3.65	0.45			
43	38.65	38.105	47.2	1.6	29.8	33.7			15.1	1.55	0.41			
43	38.26	38.65	11.6	15.1	0.8	144			1.6	0.7	0.4			
43	32.70	32.100	75.6	7.2	10.5	88			53.2	12.8	0.7			
43	26.50	26.80	48.0	14.4	3.3	143			17.6	2.6	0.6			
43	20.125	20.150	42.2	4.9	8.6	142			14.5	1.2	0.5			
43	20.95	20.125	51.9	14.5	3.6	147			26.7	1.6	0.4			
43	19.130	20.125	29.0	14.5	2.0	146			6.8	0.9	0.4			
44	32.35	32.70	11.2	53.2	0.2	na			2.8	0.9	0.6			
44	26.30	26.50	29.2	17.6	1.7	167			8.3	1.1	0.5			
44	20.70	20.95	37.7	26.7	1.4	241	3.3	1.7	15.7	3.3	0.6			
44	20.40	20.70	48.5	15.7	3.1	151			20.7	0.9	0.3			
44	18.120	19.130	86.7	6.8	12.7	94			17.3	1.4	0.5			
44	17.120	18.120	30.2	17.3	1.7	167			14.1	1.5	0.5			
					Unit 4							CP6	5/23/1978 12:00	
45	16.100	17.120	25.8	14.1	1.8	139			12.4	2.9	0.7			
46	15.100	16.100	29.3	12.4	2.4	126			9.8	1.0	0.4			
47	14.110	15.100	20.7	9.75	2.1	106	4.1	1.06	9.2	1.4	0.4			
48	13.110	15.100	28.4	9.75	2.9	105			16.4	1.3	0.4			
49	12.110	15.100	15.3	9.75	1.6	97.6			6.5	0.8	0.3			
50	11.120	12.110	10.7	6.51	1.6	66.3			5.6	1.8	0.8			
51	10.110	11.120	9.2	5.56	1.7	57.1			3.6	1.4	0.6			
52	9.110	11.120	12.2	5.56	2.2	61.4			5.4	1.7	0.7			
53	8.130	7.130	11.8	3.11	3.8	38.8			3.8	1.0	0.6			
54	6.110	7.130	26.5	3.11	8.5	46.7	4.2	0.47	8.3	0.7	0.3			
55	5.110	7.130	27.6	3.11	8.9	46.8			15.0	2.1	0.4			
56	4.130	7.130	21.6	3.11	6.9	45.5			6.80	0.89	0.29			
57	3.130	7.130	14.3	3.11	4.6	63.2			7.73	3.11	0.83			
58	2.140	7.130	24.4	3.11	7.8	46.00			12.99	3.85	0.24			
59	1.120	7.130	1.0	3.11	0.3	32.5			0.60	0.35	0.18			
													5/25/1978 12:00	

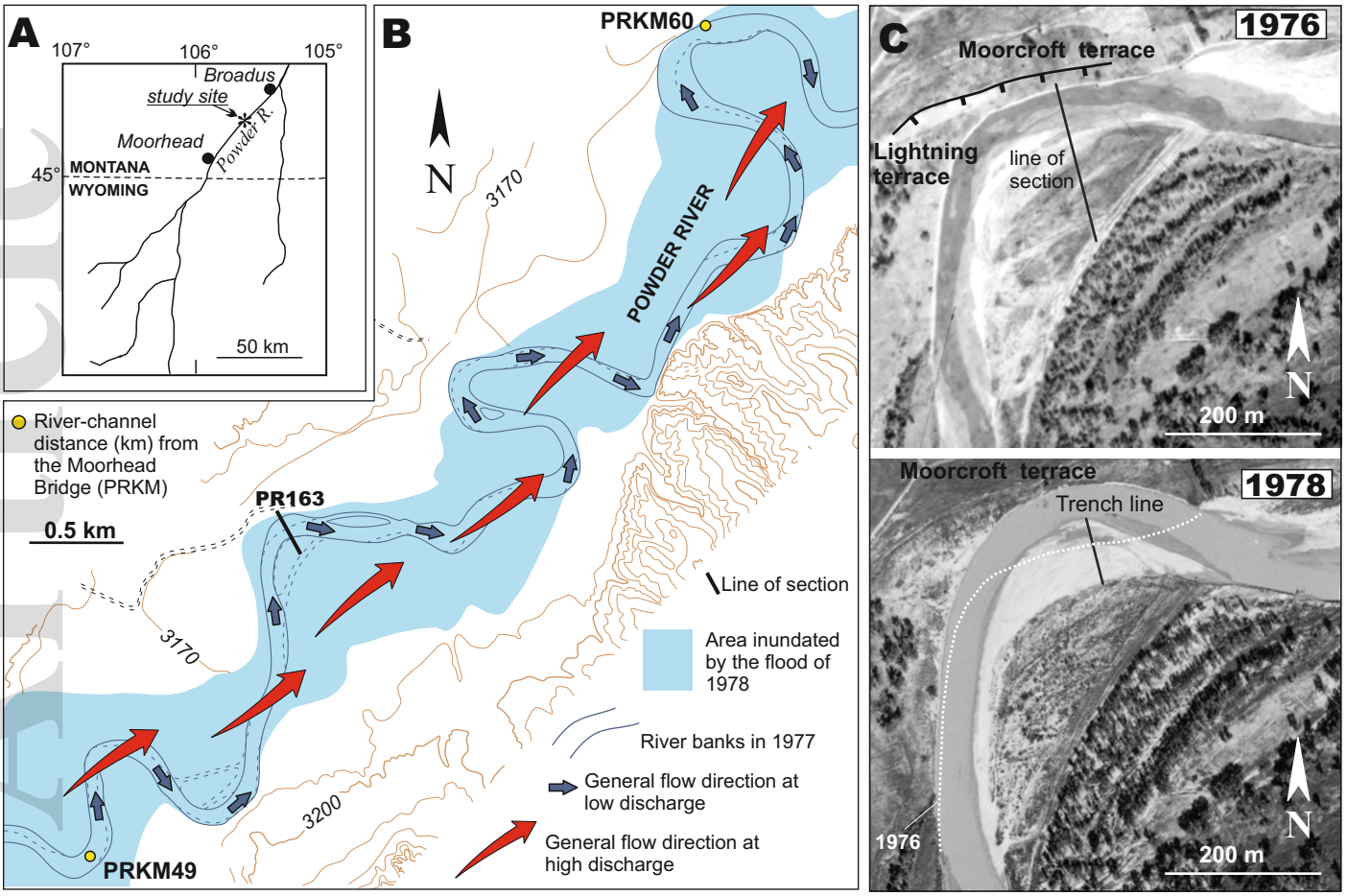

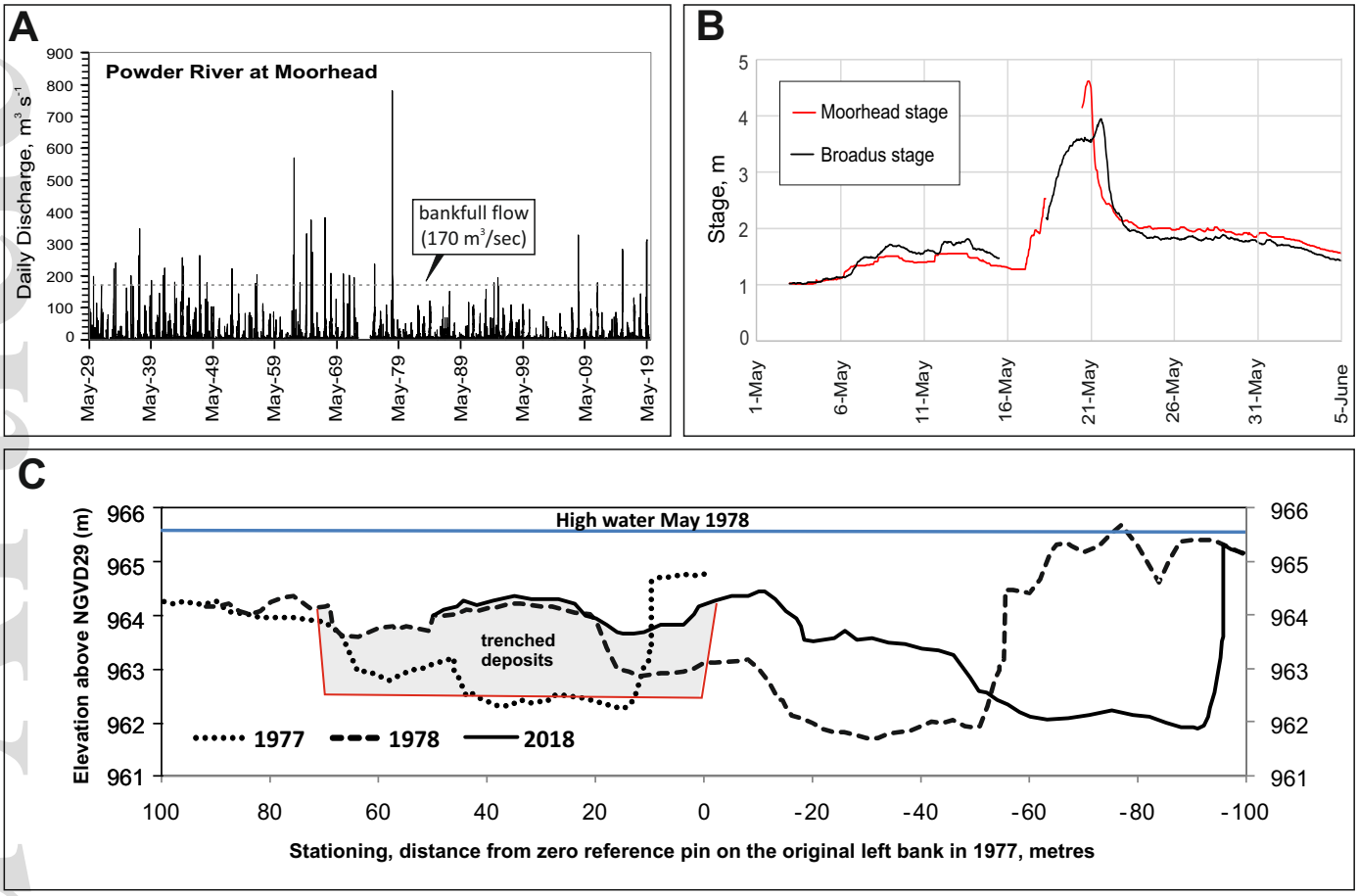

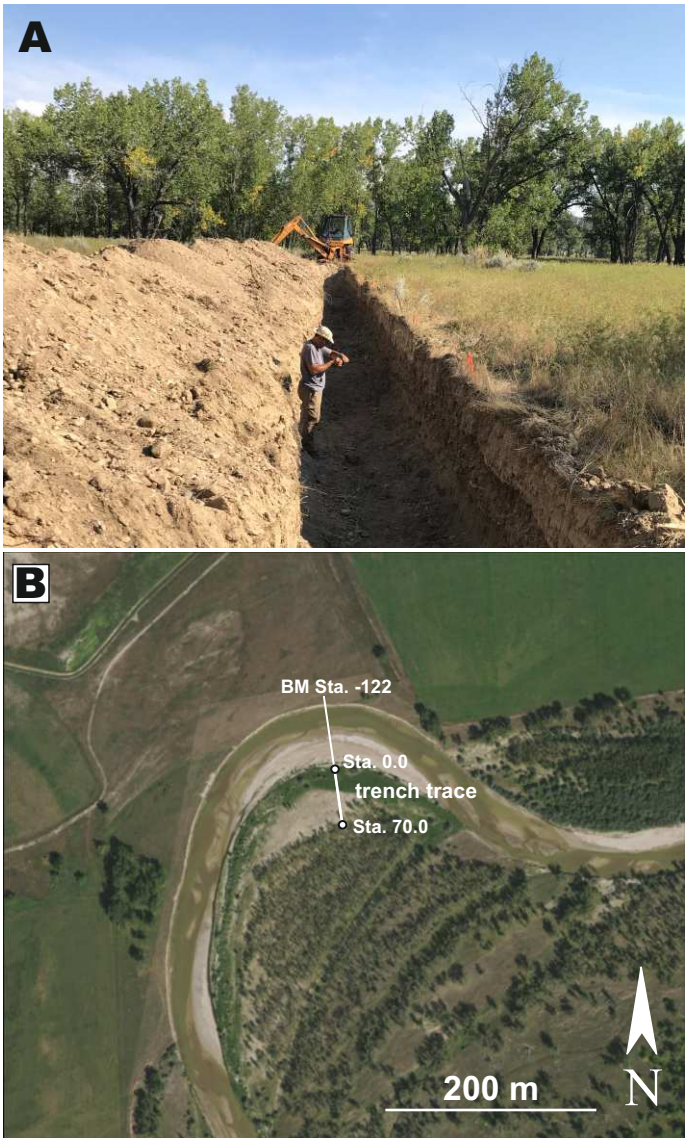

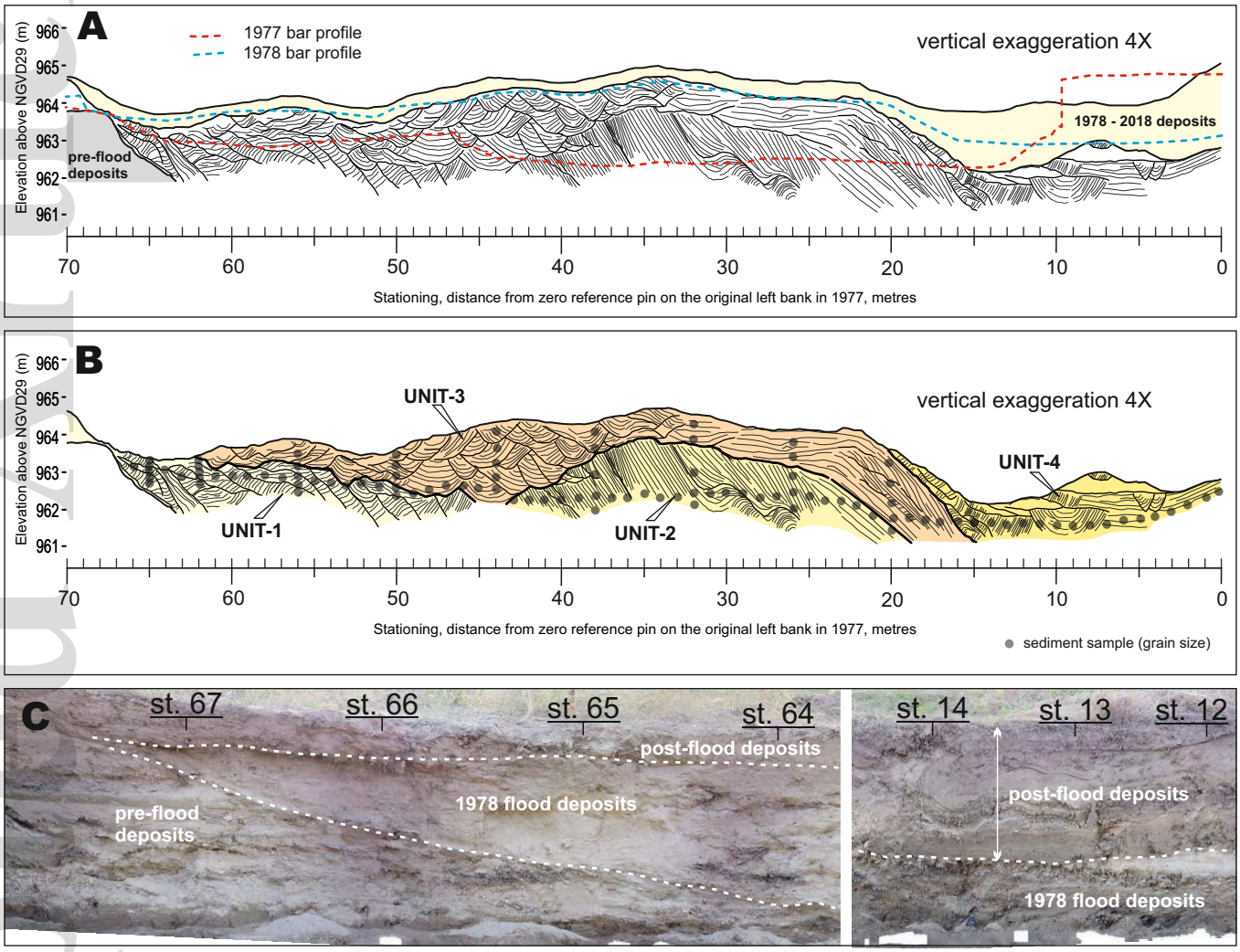

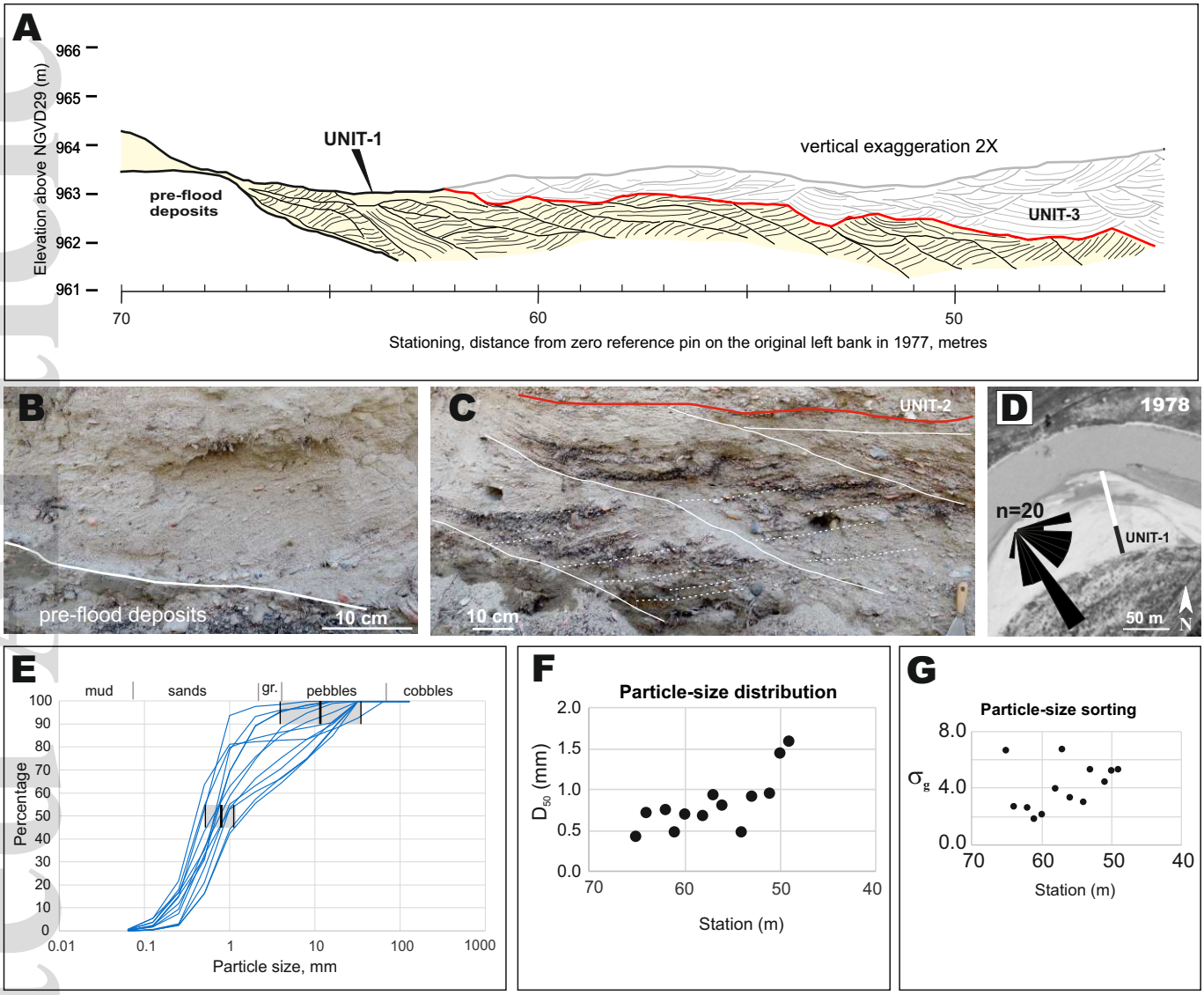

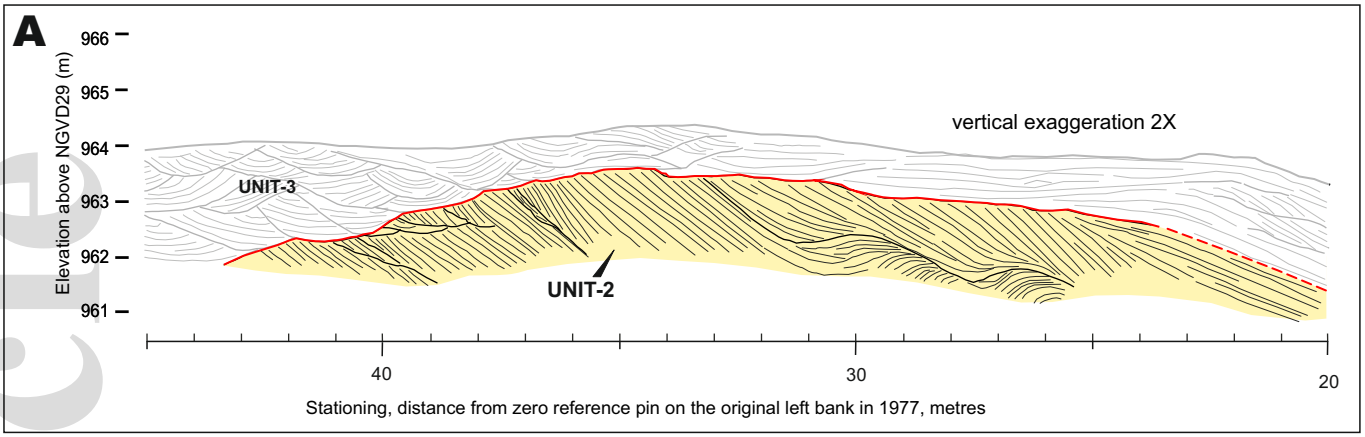

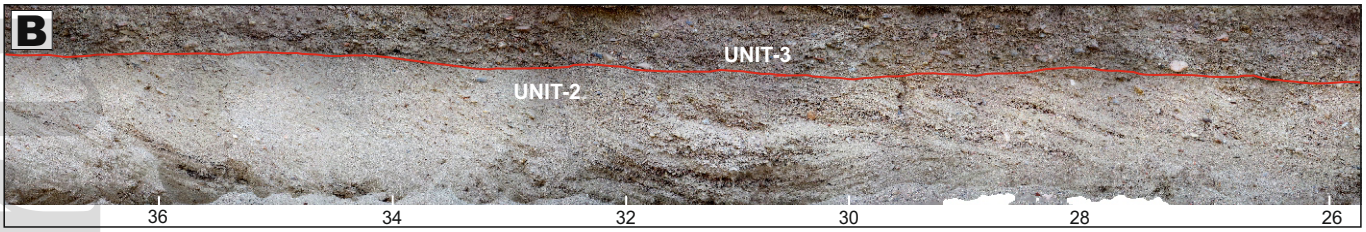

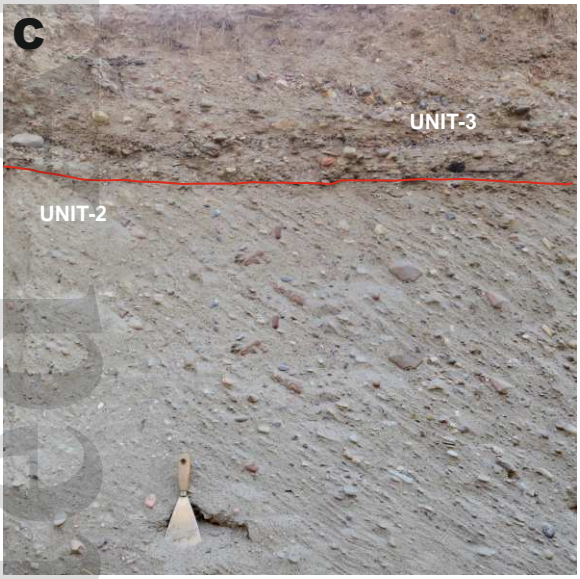

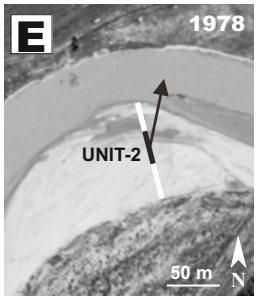

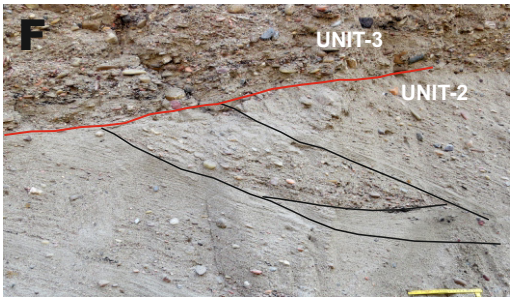

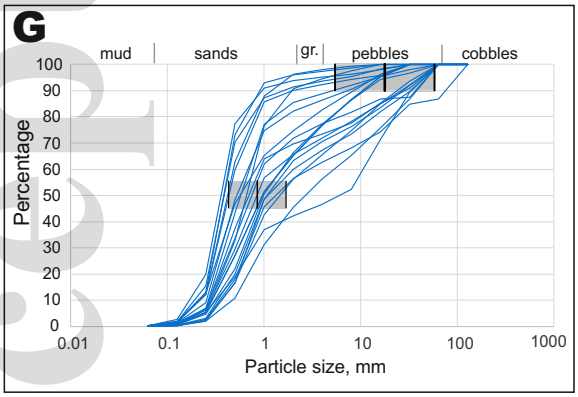

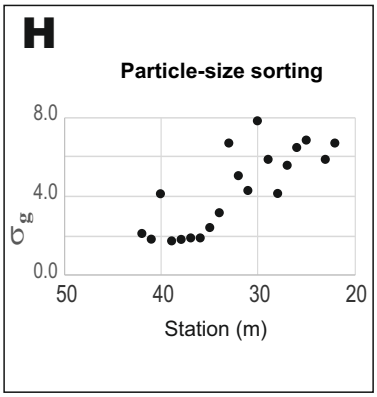

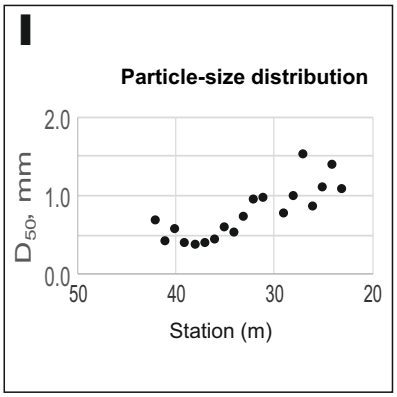

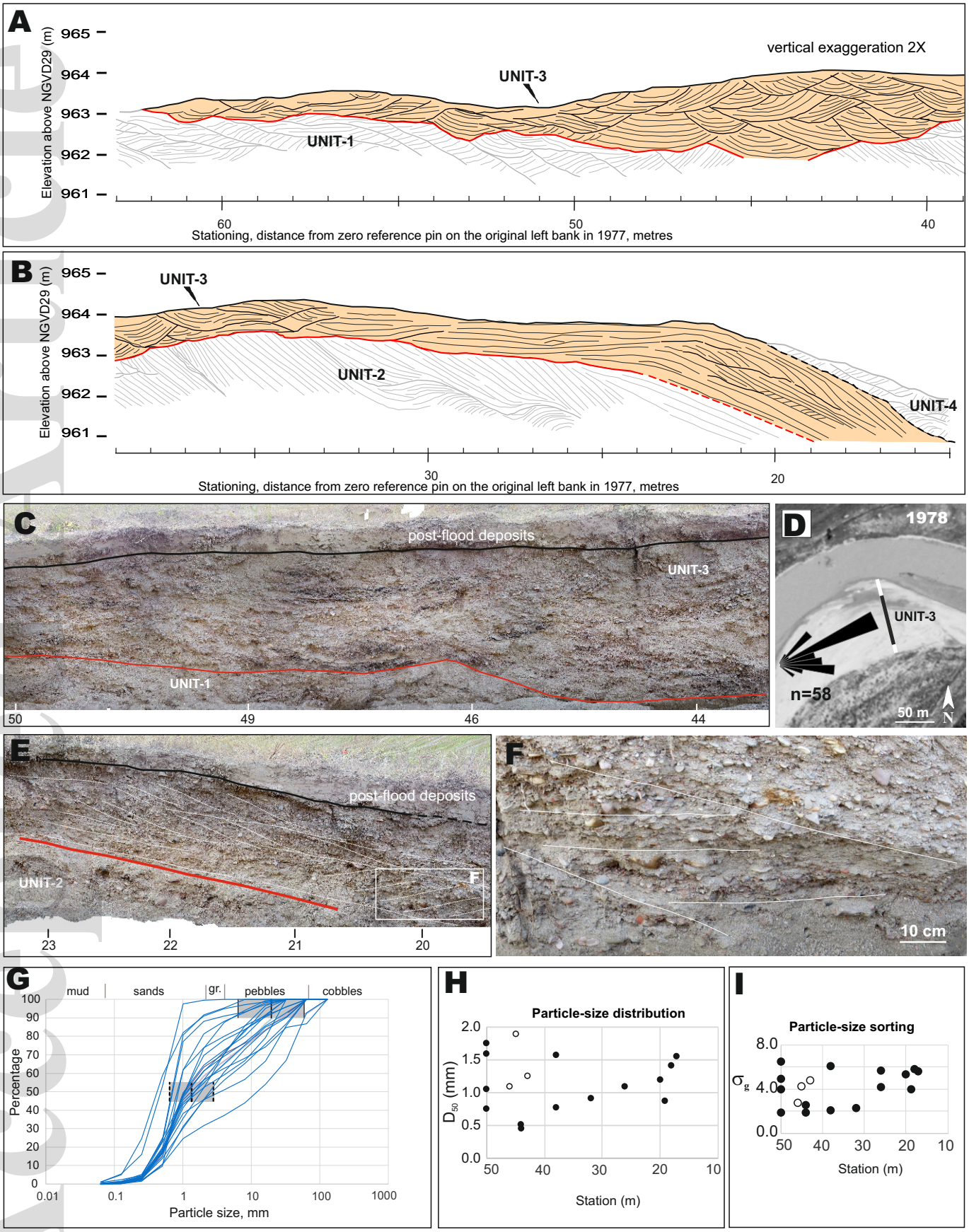

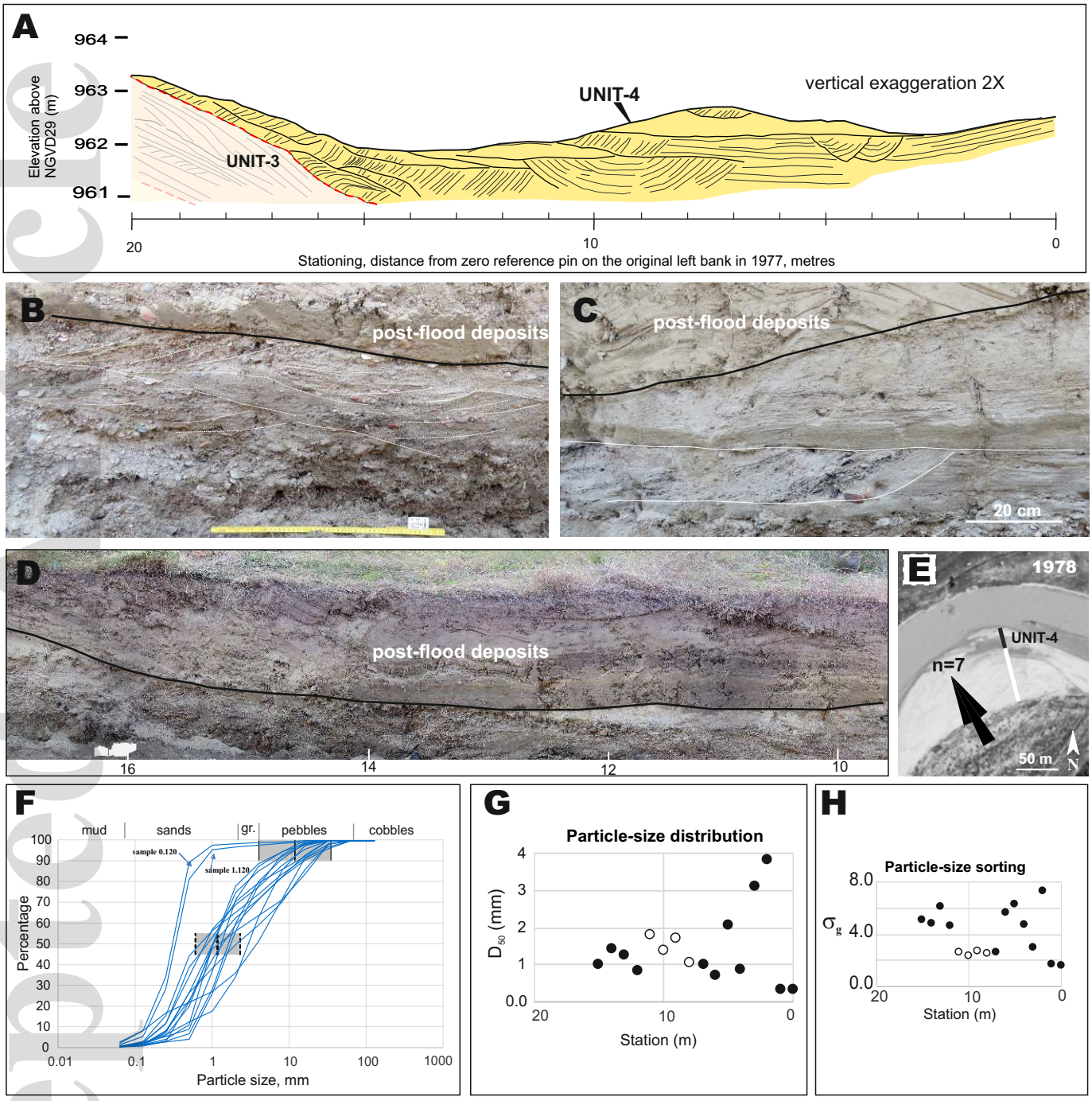

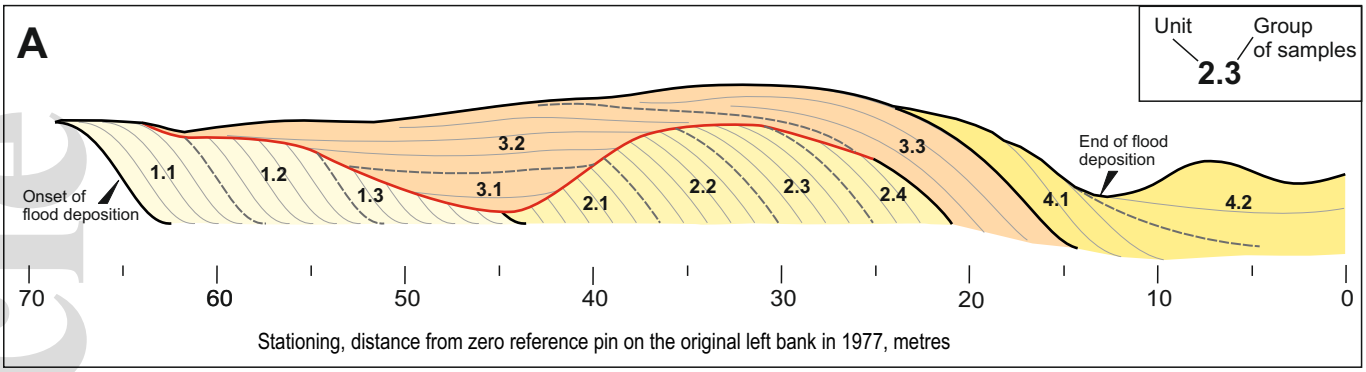

B

	Ubication	Thickness (exposed)	Grain size	Horizontal grain size trend	Vertical grain size trend	Sedimentary structures	Palaeoflow direction (Toward)	Bedding
Unit-1	Station 68 to 45	At least 120 cm	Coarse to medium-fine sand	Grain size increases moving riverward	Fining upward	Cross stratification (dominant) Plane-parallel stratification (subordinate)	SSE	350°/15-20°
Unit-2	Station 43 to 20	At least 120 cm	Coarse sand with scattered gravel	Grain size increases moving riverward	Fining upward	Single cross set (local wavy stratification)	NNE	Sub-horizontal
Unit-3	Station 60 to 16	At least 130 cm	Coarse sand with gravels	Grain size decreases moving riverward	Fining upward	Cross stratification (station 60-24) Plane-parallel stratification (station 24-16)	ENE (station 60-24) SSE (station 24-16)	Sub-horizontal (station 60-24) 350°/15-20° (station 24-16)
Unit-4	Station 20 to 0	At least 110 cm	Sand with gravels	Grain size decreases moving riverward	Fining upward	Cross- to plane-parallel stratification	SSE	350°/15-20°

C

Group	1.1	1.2	1.3	3.1	3.2	4.1
Cross-set thickness (cm)	13	26	26	22	15	7
	25	26	28	24	12	12
	14	21	27	17	31	12
	14	26	27	26	39	16
	28	19	36	19	17	24
	35	24	32	48	35	10
	23	20	34	48	30	8
	8	19	26	34	19	7
	8	19	37	21	22	26
	25	19	27	21	36	10
	15	20	32	35	23	10
	11	20		11	13	25
	12	25		22	40	11
		24		23	11	20
		17		13	30	25
		25		18	12	10
		16		13	14	19
				47	24	27
				43	19	
				44	30	
					22	
					30	
Mean cross set thickness (Sm)	17.8	21.5	30.2	27.5	23.8	15.5
Bedform height (H=2.9Sm)	51.5	62.4	87.5	79.6	69.1	45.0
Water depth (D=6.7H)	345.3	418.3	586.4	533.4	462.8	301.2
Uncertainty (50%) (D=4.4H)	226.7	274.7	385.1	350.3	303.9	197.8
Uncertainty (50%) (D=10.1H)	520.5	630.6	884.0	804.0	697.6	454.0

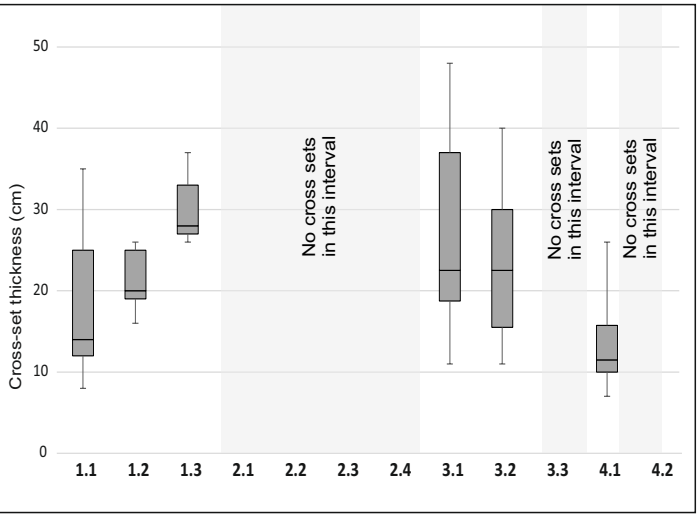

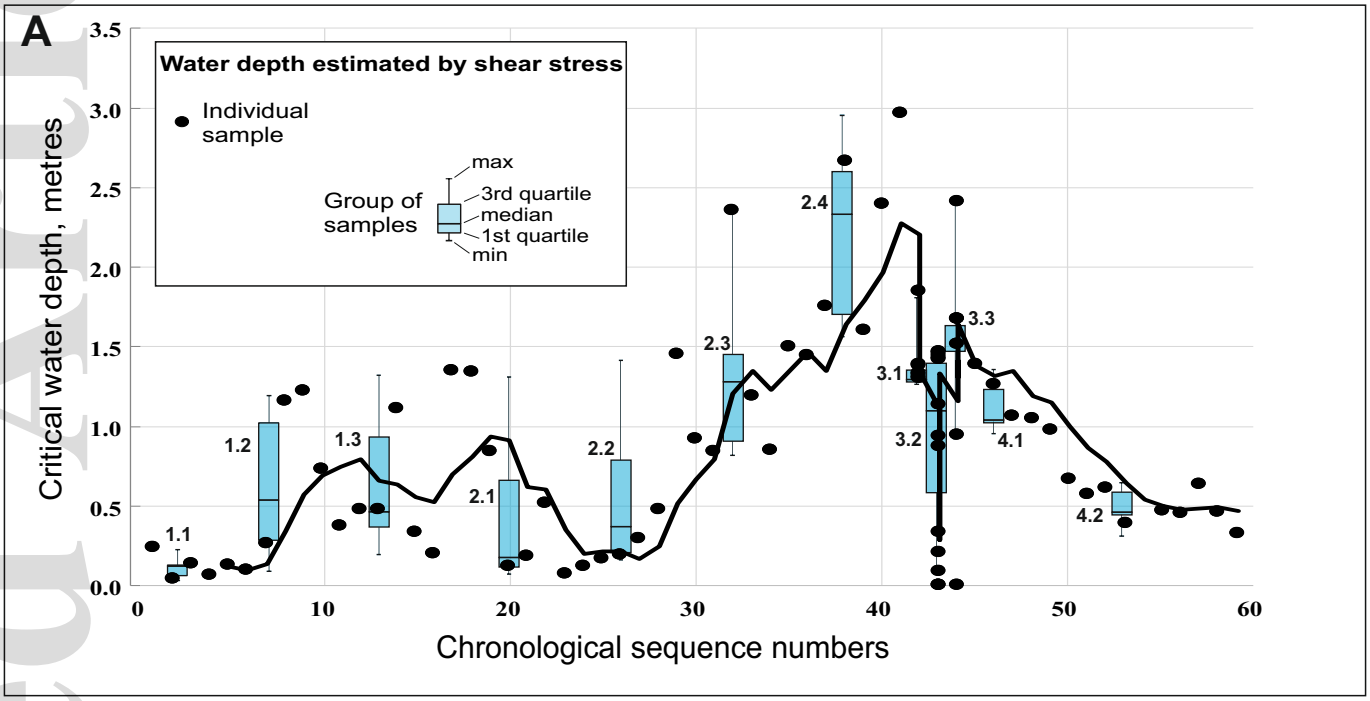

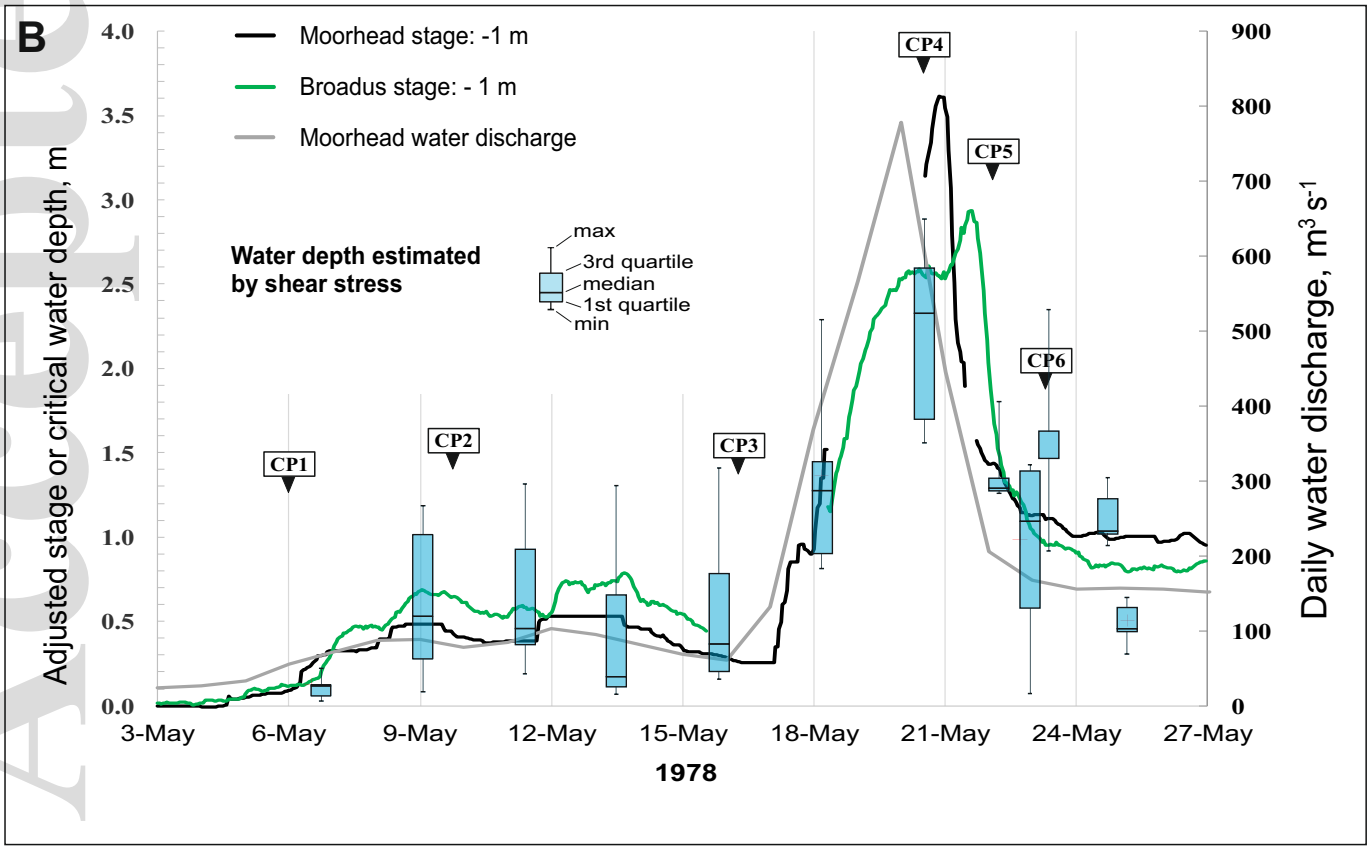

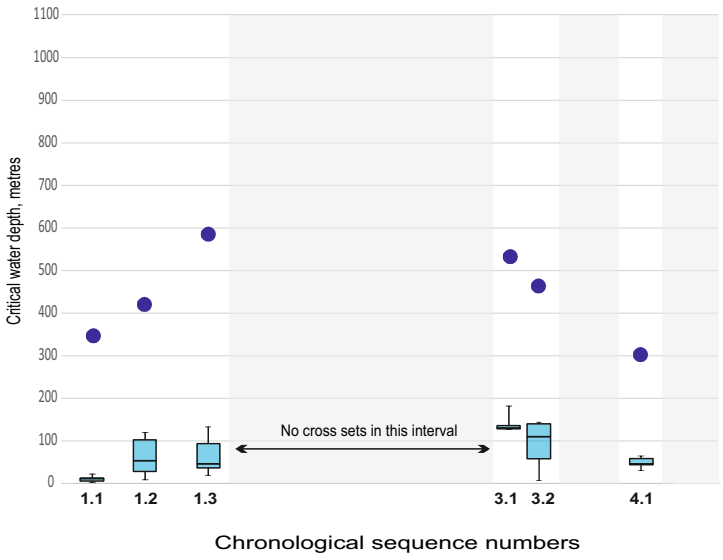

Water depth estimated by shear stress (Fig. 10)

Group of samples

max
3rd quartile
median
1st quartile
min

Water depth estimated by reconstructed mean cross-set thickness (Fig. 9C).